Manuscript Without Track Changes

Click here to access/download;Manuscript Without Track Changes;Martin et al. Brothers_FINAL_R1_CLEAN_VF.docx

Constraining temporal variations in metal and sulfur sources using high-resolution mineral-scale analysis of pyrite: evidence from the Brothers volcano, Kermadec arc, New Zealand

[1,2*]Andrew J. Martin, [2]John W. Jamieson, [3]Cornel E.J. de Ronde, [2]Graham D. Layne, [4]Glenn Piercey and Philipp A. Brandl[5]

[1] Department of Geoscience, University of Nevada, Las Vegas, USA

[2] Department of Earth Sciences, Memorial University of Newfoundland, Canada

[3] GNS Science, 1 Fairway Drive, Lower Hutt 5040, New Zealand

[4] MAF-IIC SIMS Facility, Memorial University of Newfoundland, Canada

[5]GEOMAR, Helmholtz Centre for Ocean Research Kiel, 24148, Kiel, Germany

[*]Corresponding author: Andrew.martin@unlv.edu

Keywords**:** Sulfur isotopes, trace metals, Brothers volcano, brine, magmatic volatiles

Abstract

Variations in trace metal contents and sulfur isotope ratios ($\delta^{34}S$) within pyrite, at the scale of individual mineral grains, preserves a record of temporal fluctuations in the source of metals and sulfur as well as changes in the chemical composition and temperature of hydrothermal fluid during the evolution of the Brothers volcano, Kermadec arc, New Zealand. In this study, we analyzed pyrite from drill core recovered from two geochemically distinct hydrothermal systems at the Brothers volcano, the seawater-influenced NW Caldera (Site U1530) and magmatic-volatile-dominated Upper Cone (Site U1528) during the International Ocean Discovery Program's Expedition 376. At the NW Caldera site, from 189 m below the seafloor, a seawater-derived hydrothermal fluid forming chlorite-rich alteration overprints early

pyrophyllite + illite alteration. Within ~30 m of the seafloor at this same site, pyrite contains zones of high As content with a variable $\delta^{34}S$ signature that ranges from -4.5 to 3.4‰ (*n = 26*). Values for $\delta^{34}S$ >0‰ record shallow mixing of seawater with upwelling hydrothermal fluids. In deeper parts of the system, but still within the chlorite-rich alteration zone, $\delta^{34}S$ values >0‰ are absent, indicating that relatively more sulfur is contributed from magmatic volatile degassing and SO_2 disproportionation. In the pyrophyllite-rich alteration zone, pyrite contains Co-enriched cores that correspond to sharp changes in $\delta^{34}S$ values from -5.3‰ to 4.6‰ (*n = 68*). Cobalt enrichment occurs in response to the mixing of seawater-derived hydrothermal fluid with Co-rich magmatic brines. At the Upper Cone site, a relatively constant supply of a low-salinity magmatic fluid results in pyrite grains that rarely exhibit any internal zonation in trace metal content. In pyrite where zonation does exist, a correlation between Cu and Sb and uniformly low $\delta^{34}S$ values (<0‰) indicates a link between metal enrichment, the pulsed degassing of magmatic volatiles, and SO_2 disproportionation.

Introduction

The temperature, pH and composition (e.g., salinity) of hydrothermal fluids venting at the seafloor can be influenced by dynamic magmatic processes occurring in the sub-seafloor (Rona et al. 1993; Baker 1995, 1998; Seyfried et al. 2003; Von Damm 2013). The intrusion of new magma provides a renewed source of heat to the overlying hydrothermal system, commonly leading to an increase in the temperature of fluid that is vented at the seafloor (Massoth et al. 1989; Butterfield and Massoth 1994; Von Damm, 2000). A resulting increase in fluid temperature can promote phase separation of the hydrothermal fluid if the two-phase boundary is intersected (Bischoff and Rosenbauer 1984). Phase separation produces both vapor and brine phases that can influence the transport and mobility of metals in the overlying hydrothermal system (Vanko et al. 2004; de Ronde et al. 2019a). In some instances, the intrusion of volatile-rich magmas (e.g., high in H_2O, CO_2, HCl, HF, SO_2), such as melts generated in arc-related environments, will result in the release of SO_2 that undergoes disproportionation upon cooling and mixing with the hydrothermal fluid, producing low-pH, sulfate-rich “acid sulfate” fluids (Giggenbach 1987; Kusakabe et al. 2000). Thus, the intrusion of

new magma beneath a hydrothermal system may alter the composition of hydrothermal fluids and influence the solubility, transport and deposition of metals at and below the seafloor (Seyfried and Mottl 1982; Metz and Trefry 2000).

The intrusion of new magma may also provide a direct source of some metals in the overlying hydrothermal system (Hedenquist and Lowenstern 1994; Hedenquist et al. 1994; Yang and Scott 1996). Evidence of magmatic volatile influx, especially SO_2 degassing, is widely reported in arc-hosted seafloor massive sulfide (SMS) deposits where SO_2 disproportionation produces sulfide minerals with $\delta^{34}S$ values <0‰ and sulfate minerals that have $\delta^{34}S$ values less than seawater sulfate (~21‰; Rees et al. 1978) (e.g., Conical Seamount, Gemmell et al. 2004; Hine Hina, Herzig et al. 1998; Brothers, de Ronde et al. 2005; 2011). An enrichment in Pb, As, Sb, Bi, Hg and Te (Wohlgemuth-Ueberwasser et al. 2015), Se, Au and S (Patten et al. 2020), Te, Bi, Se and Cu (Martin et al. 2021; 2022a) or Au, Te, Bi, Cu, Mo, Ag and Se (Berkenbosch et al. 2012; 2019) are also suggested as evidence of magmatic volatile influx in seafloor hydrothermal systems.

To investigate the source of metals in seafloor hydrothermal deposits, isotopic and chemical variation of hydrothermal precipitates have commonly been investigated using bulk-rock analytical methods (e.g., Herzig and Hannington 1995; Herzig et al. 1998; Fuchs et al. 2019). Bulk-rock analysis leads to the homogenization of any geochemical or isotopic variation, within the sample and across individual mineral grains (Fallick et al. 2012). Therefore, to investigate temporal variability in the composition of hydrothermal fluids during mineral precipitation, *in situ* analytical techniques that, when applied in a systematic manner (i.e., from core to rim), preserve information on spatial variation in fluid composition and metal sources (Wohlgemuth-Ueberwasser et al. 2015; Wang et al. 2018; Berkenbosch et al. 2019).

To investigate variations in fluid composition and the addition of metals from different sources, we consequently performed *in situ* analytical transects across individual pyrite grains in samples from Brothers volcano of the Kermadec arc, New Zealand. Pyrite is ubiquitous in seafloor hydrothermal systems and altered volcanic rocks from below the seafloor at Brothers (de Ronde et al. 2019a) and is a sink for many

trace metals, making it the ideal target for mineral-scale analysis (Huston et al. 1995; Butler and Nesbitt 1999; Wohlgemuth-Ueberwasser et al. 2015).

Previous studies have focused on vent field scale variations in the source of metals and sulfur (Martin et al. 2022a) or only analyzed samples collected at the seafloor from Brothers (de Ronde et al. 2005, 2011). These studies have identified links between magmatic volatile influx and the enrichment of Te, Se, Cu and Bi and have shown that sulfur is contributed from magmatic volatile degassing and SO_2 disproportionation. However, no consideration has been given to how or indeed if the source of metals and sulfur changes over time.

In this study, using samples that were collected from the deep-sea drilling of the Brothers volcano during the International Ocean Discovery Program's Expedition 376: "Brothers Arc Flux" (de Ronde et al. 2019b, c), we employ a combined analytical approach utilizing both geochemical mapping and sulfur isotope ratios. This approach allows links to be established between metal enrichment processes and the source of sulfur, and when combined with detailed petrography, determine temporal variations that occurred as the pyrite grains grew. We show that traditional bulk-rock analysis and *in situ* analyses that do not employ a systematic analytical approach (i.e., from core to rim), underestimate the complexity of mineralizing processes at Brothers. The source of metals and sulfur fluctuates considerably during pyrite growth and preserves evidence of brine dilution, seawater mixing and magmatic volatile degassing.

Brothers volcano

Geology

Brothers volcano is located in the southern part of the Kermadec-Tonga interoceanic arc, NE of New Zealand (Fig. 1A). The volcano consists of an elongate, northwest-southeast aligned edifice with a prominent caldera measuring ~3 x 3.4 km at its lower rim (Fig. 1B and C; Embley et al. 2012). In the southern part of the caldera, a younger cone has formed (Fig. 1C). The volcanic rocks at Brothers are dominated by dacites (Haase et al. 2006; Timm et al. 2012; Wysoczanski et al. 2012; Brandl et al., 2023).

Both on and below the seafloor, volcanic host rocks locally have a prominent brecciated texture and are variably-altered to assemblages of secondary minerals that formed during the interaction of magmatic-hydrothermal fluids with volcanic host rocks (de Ronde et al. 2005; de Ronde et al. 2019a; Martin et al. 2022b).

Hydrothermal venting

The Brothers caldera hosts five active and one inactive site of hydrothermal venting (de Ronde et al. 2005; Baker et al. 2012; Stucker et al. 2022). In this study we focus on two of the active sites: the Upper Cone (Site U1528) and NW Caldera (Site U5130; Fig. 1B and C). These sites have vent fluid compositions that are influenced by magmatic volatile degassing and seawater-derived hydrothermal fluids, respectively (de Ronde et al. 2011; 2019a, b, c; Stucker et al. 2022). At the Upper Cone site, hydrothermal fluids venting at the seafloor are low-temperature (up to 122°C), highly acidic (pH 1-2) and contain elevated ΣSO_4 (up to 88.9 mM) and H_2S (5.0 mM) (de Ronde et al. 2011; Kleint et al. 2019; Stucker et al. 2022). At the seafloor, venting is diffuse and Fe-oxide crusts and chimneys comprised of native sulfur are common (de Ronde et al. 2011, 2005). By contrast, fluid venting at the NW Caldera site is high-temperature (up to 320°C), moderately acidic (pH 3-4), and gas-poor, but contains elevated Cl concentrations (up to 751 mM) and low H_2S contents (1.1 mM) (de Ronde et al. 2011; Kleint et al. 2019; Stucker et al. 2022). Fluid venting at the NW Caldera occurs along a series of ring faults on the caldera wall (Embley et al. 2012) forming metal-sulfide-rich black smoker chimneys (de Ronde et al. 2005; Berkenbosch et al. 2012).

Alteration mineralogy

The alteration mineralogy of samples is distinct between the Upper Cone (Site U1528) and NW Caldera (Site U1530) (de Ronde et al. 2019a, b, c; Martin et al. 2022b). At the Upper Cone, two different alteration assemblages have been identified: natroalunite ± pyrophyllite-rich samples, indicating high-temperature (>300°C) low-pH fluids (~1-3), and samples that contain smectite indicating lower temperature (~180°C) and near neutral pH fluids (~4-5) (de Ronde et al. 2019a, b; Martin et al. 2022b). The two mineral

assemblages occur intercalated at irregular intervals from the seafloor to the bottom of the drill hole (359.3 meters below seafloor (mbsf); de Ronde et al. 2019b). The irregular distribution of alteration minerals with depth below the seafloor indicates that acid sulfate fluids were locally channeled along discrete permeability pathways forming natroalunite-rich alteration, whilst smectite-rich zones represent regions of increased seawater influx (de Ronde et al. 2019b).

At the NW Caldera (Site U1530), a further two alteration mineral assemblages have been identified. The first assemblage occurs from the seafloor to the bottom of the drill hole (453. 1 mbsf) and contains chlorite + quartz (de Ronde et al. 2019c). The second assemblage contains pyrophyllite + illite (with diaspore and zunyite) and only occurs in the lower part of the drill hole from 189 mbsf to the bottom of the hole (453.1 mbsf). Chlorite + quartz alteration formed during the interaction of high-temperature (>300°C), moderately acidic (pH 3-4) seawater-derived hydrothermal fluids with volcanic host rocks (de Ronde et al. 2019a, c; Martin et al. 2022b). By contrast, pyrophyllite + illite alteration formed at a lower pH (1-3) from high-temperature (>320°C) fluids derived from magmatic volatile degassing (de Ronde et al. 2019a, c; Martin et al. 2022b). Below a depth of 189 mbsf, chlorite + quartz alteration overprints older pyrophyllite + illite alteration and is related to changes in subsurface permeability that occurred during caldera collapse (de Ronde et al. 2019a). We retain the use of these alteration mineral assemblage classifications throughout this study.

Sulfur isotope systematics

At the Upper Cone, bulk sulfur isotope ratios ($\delta^{34}S$) of pyrite from the seafloor average -4.5 ± 0.6‰ (1σ, *n = 4*; de Ronde et al. 2005). Pyrite analyzed from below the seafloor is more variable with an average $\delta^{34}S$ value of -6.4 ± 2.8‰ (1σ, *n=7*) for samples containing smectite, and -5.2 ± 2.9‰ (1σ, *n = 24*) for samples containing natroalunite ± pyrophyllite (Martin et al. 2022a). Natroalunite and native sulfur from the seafloor at this site have an average $\delta^{34}S$ value of 16.3 ± 1.4‰ (1σ, *n=4*) and -5.8 ± 2.1‰ (1σ, *n = 9*), respectively. Here, H_2S from vent fluid has an average $\delta^{34}S$ value of -3.6 ± 2.1 (1σ, *n = 4*) (de Ronde et al. 2003, 2011). The predominance of $\delta^{34}S$ values in pyrite and natroalunite that are lower than the magmatic host rocks

(~5‰, enriched arc mantle; Ueda and Sakai 1984) and seawater (~21‰; Rees et al. 1978) respectively, indicate that SO_2 disproportionation is widespread at the Upper Cone site (de Ronde et al. 2005; 2011).

Analysis of pyrite from sulfide chimneys and sulfide-rich breccia at the seafloor from the NW Caldera yields an average $\delta^{34}S$ value of -1.2 ± 2.0‰ (1σ, *n = 24*; de Ronde et al. 2003, 2005, 2011). The sulfur isotope composition of barite from the same chimneys averages 21.3 ± 0.8‰ (1σ, n = *20*; de Ronde et al. 2011). Pyrite from chlorite + quartz-rich alteration from below the seafloor has an average $\delta^{34}S$ composition of -4.6 ± 3.5‰ (1σ, *n* = 26) and pyrophyllite + illite samples average -4.8 ± 5.5‰ (1σ, *n = 20*) (Martin et al. 2022a). The sulfur isotope composition of sulfate and sulfide minerals at the NW Caldera indicate that sulfur is sourced from the leaching of igneous host rocks, thermochemical sulfate reduction (TSR) of seawater and the disproportionation of degassing SO_2 (de Ronde et al. 2005, 2011). However, temporal variation in the relative source(s) of sulfur at Brothers are poorly constrained, as are links between the source of sulfur and the trace metal enrichment signature of pyrite.

Trace metal signatures in pyrite

A previous study utilized laser ablation inductively coupled plasma mass spectrometry (LA-ICP-MS) analysis of pyrite from below the seafloor at the NW Caldera and Upper Cone sites. The aim of the study was to investigate borehole-scale variation in the source of metals and sulfur within and between the different vent sites at Brothers (Martin et al. 2022a). Pyrite from pyrophyllite ± natroalunite samples at both the NW Caldera and Upper Cone are enriched in Cu, Se, Te, Co and Bi, indicating a link between magmatic volatile degassing and the enrichment of these elements (Martin et al. 2022a). By contrast, pyrite from chlorite + quartz-rich alteration at the NW Caldera is depleted in Cu, Te and Bi indicating that these metals were leached during later seawater overprinting. At the NW Caldera, pyrite in samples at or within, 30 m of the seafloor contain elevated Ag, Sb, and As contents, due to lower fluid temperatures associated with shallow sub-surface seawater mixing (Martin et al. 2022a). In addition to changes in the trace metal content of the pyrite, Martin et al. (2022a) documented different types of internal zonation within the pyrite grains. Pyrite grains from chlorite-rich alteration near the seafloor at the NW Caldera exhibited oscillatory

overgrowths, whilst pyrite from deeper samples contained oscillatory zonations that delineated relict core zones. In contrast, comparable zonations were generally absent at the Upper Cone site and pyrite did not commonly exhibit any internal zonation (Martin et al. 2022a). To investigate the origin and significance of these zonations in the context of an evolving magmatic-hydrothermal system at the Brothers volcano, we undertook element mapping and high-resolution mineral-scale analytical transects allowing correlations between sulfur isotope ratios and the distribution of trace metals to be investigated.

Methods

Sample collection

Samples in this study were collected during IODP Expedition 376: "Brothers Arc Flux" aboard the D/V *JOIDES Resolution* (de Ronde et al. 2019b, c). We analyze samples from two drill sites: the Upper Cone (IODP Site U1528, Hole U1528D) and the NW Caldera (Site U1530, Hole U1530A; Fig. 1B). Drilling at the Upper Cone site penetrated to a maximum depth of 359.3 mbsf with an overall core recovery of 29.3% (de Ronde et al. 2019b). At the NW Caldera, drilling penetrated to a maximum depth of 453.1 mbsf, with an overall core recovery rate of 16.9% (de Ronde et al. 2019c).

Etching of sulfide grains

Prior to geochemical analysis, pyrite was etched with sodium hypochlorite (1% NaOCl) to reveal any internal variations. Samples were etched for 90 s, rinsed with water and then air-dried. This process tarnishes the pyrite to expose zonations, sub-grain boundaries and mineral inclusions that are then imaged using reflected light microscopy (Cox et al. 1981; Cox 1987; Tanner et al. 2016). Etching provides a low cost and rapid way to assess the internal morphology of pyrite grains. The tarnish was later easily removed using 0.25 μm diamond polishing solution and a polishing pad.

Geochemical Mapping

Electron probe micro-analysis (EPMA) was used to qualitatively map trace metal distribution in pyrite. Arsenic, Co, Cu, Se, and Sb were analyzed using a JEOL JXA-8230 SuperProbe equipped with five wavelength-dispersive spectrometers at Memorial University of Newfoundland (Canada). The instrument operated at an accelerating voltage of 20 KeV, a beam current of 250 nA and a dwell time of 200 ms. The resolution of maps depended on the size of the mineral grain analyzed but was typically ~1 μm per pixel.

Sulfur isotope analysis

The sulfur isotope composition ($\delta^{34}S$) of pyrite was determined using Secondary Ion Mass Spectrometry (SIMS) microanalysis. In total, 10 pyrite grains from seven representative polished mounts were analyzed employing closely spaced analytical transects of points (*n = 134*) from the grain core to rim with an additional 15 analyses performed on primary magmatic sulfide blebs from unaltered volcanic rocks. Sample blocks were mounted in epoxy in aluminum retaining rings, polished, and coated with 300Å of Au prior to analysis to mitigate charging of the sample during ion bombardment. Samples were analyzed using a Cameca IMS 4f SIMS instrument at the CREAIT Microanalysis Facility at Memorial University of Newfoundland (Canada) following the analytical procedure outlined in Brueckner et al. (2015). Each sample was bombarded with a primary beam of 250-750 pA of Cs^+, accelerated through a potential of 10 keV, and focused into a 10 μm diameter beam. Negatively charged sputtered secondary ions were accelerated into the mass spectrometer using a potential of +4.5 keV. The duration of each analysis was 16.3 minutes including 120 seconds of pre-sputtering with a 10 μm square raster applied to the beam spot to remove sulfur contamination from the sample surface. Reproducibility, based on the repeat analysis of pyrite-UL9 ($\delta^{34}S$= 16.3‰), was better than ±0.4‰ (1σ) (see ESM, Table A1). Internal precision on individual sample spots was typically better than ±0.4‰ (1σ). All analyses are reported in standard delta notation relative to Vienna-Canyon Diablo Troilite (V-CDT).

Results

Sample characterization

We present isotopic and geochemical data from 10 pyrite grains from core sections that represent the major alteration mineral assemblages present at Brothers volcano (Martin et al., 2022b). The pyrite grains selected contain a representative suite of different internal zonation patterns identified from a larger etching study. Hence, the 10 pyrite grains selected for detailed analysis are considered to be representative of a wide range of hydrothermal processes occurring at the Brothers volcano.

Upper Cone (Site U1528)

To classify alteration mineral assemblages in this study, we retain the use of the original classification outlined by de Ronde et al. (2019a) and Martin et al. (2022b). Two samples were analyzed from the Upper Cone (Fig. 2A; ESM, Table A2). Core section 23R1, from 162.5 mbsf, is a volcanic breccia that has been altered to an assemblage of natroalunite + pyrophyllite + anhydrite + pyrite and quartz (Fig. 2B). Clasts appear less-altered, variably resorbed, and darker in color than the surrounding matrix, which is white and contains native sulfur (Fig. 2B). Core section 49R2 was collected from 287.3 mbsf; it is pervasively altered with a massive texture and contains no visible clasts (Fig. 2C). It is composed of smectite + anhydrite + pyrite + quartz with natroalunite and cristobalite. Pyrite in both samples occurs as fine-grained (<0.2 mm) disseminated euhedral to subhedral grains (Fig. 2B-1 and C-1).

NW Caldera (Site U1530)

Five representative samples were analyzed from the NW Caldera (Fig. 3A; ESM, Table A2). Core section 1R1 is located at the seafloor (0.1 mbsf); the sample has a prominent brecciated texture with angular blue-green clasts that are chlorite and illite-rich in a matrix of pyrite + anhydrite + barite and minor (<5 vol.%) sphalerite (Fig. 3B). Pyrite (and minor marcasite) occur as coarse-grained aggregates, with pyrite often exhibiting growth zonations defined by regions of increased porosity (Fig. 3B-1). Core section 5R1 is located at a depth of 25.9 mbsf; the sample has a brecciated texture with blue-green illite-chlorite-rich clasts

in a matrix of pyrite, anhydrite and barite with sphalerite (Fig. 3C). Pyrite occurs in the matrix as aggregates of euhedral-disseminated grains (Fig. 3C-1).

Core section 55R1 is located at a depth of 265.9 mbsf and contains quartz + pyrophyllite + anhydrite + diaspore and rutile with a mottled equigranular texture, and is crosscut by an anhydrite vein (Fig. 3D). Pyrite occurs as disseminated anhedral grains (Fig. 3D-1). Core section 65R1 is located at a depth of 313.9 mbsf and contains quartz + anhydrite + pyrophyllite, diaspore and rutile (Fig. 3E). Pyrite forms disseminated grains with an anhedral morphology (Fig. 3E-1). Core section 83R1 is located at a depth of 400.3 mbsf and contains chlorite, anhydrite and quartz (Fig. 3F). Pyrite is disseminated throughout the sample and forms discrete aggregates of euhedral grains (Fig. 3F-1).

Sulfide etching

Pyrite grains show a range of different internal morphologies when etched with NaOCl (Fig. 4). Pyrite from the Upper Cone (Fig. 4A) generally exhibited less internal color variation than pyrite at the NW Caldera. At the Upper Cone, etching was useful in delineating the boundary between different sub-grains in aggregates of fine-grained euhedral pyrite (Fig. 4B). Internal zonations are rarely present, and generally occur parallel to the grain margin and define oscillatory overgrowths (Fig. 4C).

At the NW Caldera, three different forms of internal variation are commonly observed. The first type is characterized by minimal changes in color across zones, with zonations appearing as black lines or darker horizons that are parallel to the current grain margin (Fig. 4D). The second type of variation consists of sharp changes in color (e.g., blue to yellow) with clear growth zones that exhibit a different orientation to the present grain margin (Fig. 4E). The third type of variation consists of irregular very-fine (<10 μm) bright bands that do not exhibit any correlation with respect to the core or rim of the grain and have no preferred orientation (Fig. 4F).

Sulfur isotopes

Upper Cone

Pyrite from core section 23R1 (Fig. 5A-1) shows clear oscillatory growth zones emanating from the core of the grain with a later overgrowth of pyrite (blue-yellow; Fig. 5A-2). Eighty-eight percent of $\delta^{34}S$ values fall within ±1σ of the median value (-1.4‰) (Table 1; Fig 5A-3). The grain center is enriched in ^{34}S relative to the grain margin and there is no distinct isotopic composition associated with each of the three growth zones (Fig. 5A-3).

The median $\delta^{34}S$ value of -5.9‰ for core section 49R2 (289 mbsf) is notably lower than the pyrite grain analyzed in core section 23R1 (164 mbsf; Table 1). The grain has no visible zonations and contains a region that is rich in anhydrite inclusions that has the lowest $\delta^{34}S$ values (Fig. 5B-1 and B-2). The core of the grain is slightly enriched in ^{34}S relative to the grain margin and 71% of analyses fall within ±1σ of the median value (-5.9‰) (Fig. 5B). Similar to the sample shown in Figure 5A, sample 5B also shows a ~4‰ range in $\delta^{34}S$ values.

NW Caldera – Chlorite + quartz alteration

Pyrite from core section 1R1 exhibits a complex oscillatory zonation pattern with an inner core zone (Fig. 6A-1 and A-2). Only 58% of data plot within ±1σ of the median value (-1.1‰) (Table 1; Fig. 6A-3). The grain core and innermost zone are depleted in ^{34}S with respect to the surrounding outer zone, with $\delta^{34}S$ values decreasing toward the grain margin (Fig. 6A-3).

Two pyrite grains were analyzed in core section 5R1 (Table 1). The first pyrite grain contains a homogenous euhedral core that has been overgrown by a later pyrite generation that exhibits oscillatory zonations (Fig. 6B-1 and B-2). The core of the inner euhedral grain is enriched in ^{34}S up to 3.4‰, as is the region that appears blue to yellow in color in Figure 6B-2 (up to 2.4‰). The outermost margin of the grain contains the lowest $\delta^{34}S$ values down to -2.2‰ (Fig. 6B-3). The second pyrite grain has a euhedral morphology and

exhibits oscillatory zonations with the core appearing blue-yellow in color (Fig. 6C-1 and C-2). The core is enriched in ^{34}S relative to the grain margin (Fig. 6C-3).

Pyrite from core section 83R1 (Fig. 6D-1) contains two sub-grains defined by the ochre and yellow color in Figure 6D-2. The larger ochre colored grain exhibits weak oscillatory zonations that are sub-parallel to the grain margin (Fig. 6D-2). The median $\delta^{34}S$ composition of the grain is -4.0 ± 3.8‰ (1σ, *n = 16*; Table 1); this is notably less than other near-seafloor pyrite from chlorite-rich alteration (1R1 and 5R1). The $\delta^{34}S$ values decrease across the grain with no clear correlation from the core to the rim, with, for example, opposing grain edges containing $\delta^{34}S$ values of -0.8‰ and -7.5‰, respectively (Fig. 6D-3).

NW Caldera – Pyrophyllite + illite alteration

Pyrite analyzed from pyrophyllite + illite alteration has a notably larger inter-grain range in $\delta^{34}S$ values (13.5‰) compared to pyrite analyzed from chlorite + quartz alteration (8.0‰; Table 1). The etching of sample 55R1 showed complex internal variations (Fig. 7A-1 and A-2). The zonations, defined by brighter orange regions, appear random in shape and orientation (see also Fig. 4F). Values of $\delta^{34}S$ >0‰ are absent in sample 55R1, with 79% of data falling within ±1σ of the median value (-3.2‰) (Table 1; Fig. 7A-3). There is no clear correlation between $\delta^{34}S$ values and the location of the analytical point within the grain, nor is there any correlation between brighter regions and sulfur isotope ratios.

Etching of pyrite in sample 65R1-A reveals the presence of a relict core defined by oscillatory zonations of orange with a sub-grain located at the margin of the grain (Fig. 7B-1 and B-2). Zonations occur as complex orange bands that are sub-parallel to the current grain margin (Fig. 7B-2). The core of the grain is enriched in ^{34}S relative to the grain margin, with both low (-5.4‰) and high (+3.8‰) $\delta^{34}S$ values recorded at the margin of the grain (Fig. 7B-2 and B-3). A detailed transect across the core of the same grain (Fig. 7C-1) shows comparatively large positive (up to 4.1‰) and negative (down to -2.1‰) excursions in $\delta^{34}S$ values (Fig. 7C-2). A sharp transition in $\delta^{34}S$ values, from 4.1‰ to -2.1‰ occurs at the brightest visible band moving from the rim toward the core of the grain (Fig. 7C-3). In grain 65R1-B, a square-shaped core characterized by orange oscillatory zonations is visible (Fig. 7D-1 and D-2; lower right hand corner). The

sulfur isotopic composition of the grain shows a symmetrical profile with the core enriched in ^{34}S (up to 1.2‰) relative to the margin of the grain (Fig. 7D-3). Pyrite from sample 65R1-C is anhedral (Fig. 7E-1) with internal zonations delineated by bright orange regions (Fig.7E-2). The zonations define a core region but occur sub-parallel to the current grain margin (Fig. 7E-2). The range in $\delta^{34}S$ values (-5.3 to 4.6‰) is comparable to samples 65R1-A and B (Table 1). A shift from 1.9‰ to -5.2‰ occurs as the second bright band is intersected moving from the core to rim of the grain (Fig. 7E-3).

Magmatic sulfide blebs

To establish the sulfur isotopic composition of host rocks at Brothers, we analyzed magmatic sulfide droplets, with a stoichiometric composition similar to pyrrhotite (i.e., Monosulfide Solid Solution – MSS), in unaltered samples (ESM 3). Their size and texture ranges from small (15-45 µm) sulfide droplets to large (120-150 µm) sulfide-magnetite clusters (ESM, Table A2), with grains having a comparable morphology to magmatic sulfide minerals previously described at Brothers (Keith et al. 2018; Brandl et al., 2023). The median $\delta^{34}S$ value for MSS-type inclusions was 0.2‰ ($n=15$) with an average of 0.9±2.4‰ ($n=15$, 1σ) and a range of -3.1‰ to 6.7‰ (Table 1).

Trace metal mapping

The mineral-scale distribution of As, Cu, Co, Se and Sb between different pyrite grains from altered volcanic rocks below the seafloor at Brothers volcano is highly variable. At the Upper Cone, sample 23R1 shows concentric zonations in Cu and Sb content, with high contents along distinct growth zones (Fig. 8A and B). The distribution of Se, As and Co is homogenous with no zonation visible in the grain (Fig. 8C, D and E).

At the NW Caldera, core section 1R1 shows zonations in As content, with the highest As occurring along crystal growth boundaries (Fig. 9A). The core of grain 1R1 appears relatively enriched in As compared to surrounding overgrowths. The distribution of Sb is similar to As, with the highest content occurring along growth zones at the margin of the grain (Fig. 9B). Copper exhibits weak zonation and is concentrated along

growth zones, but also occurs as micron-scale inclusions of chalcopyrite (Fig. 9C). Selenium and Co do not exhibit any zonation (Fig. 9D and E). In sample 5R1 (grain A and B), As is strongly enriched at the contact between early euhedral pyrite and later pyrite overgrowths (Fig. 9F) and corresponds to blue-yellow colors in the etched image (Fig. 6B and C). Antimony, Se and Co do not show any detectable variation (Fig. 9G, I, J). The distribution of Cu exhibits only minor variation as bright bands in the late pyrite overgrowths (Fig. 9H).

High-Co content in pyrite from sample 55R1 occurs as randomly distributed micron-scale zones (Fig. 10A). Arsenic, Cu, Se and Sb are homogenously distributed (Fig. 10B to E). The distribution of Co is highly heterogeneous in pyrite 65R-1A (Fig. 10F and F*). Increased Co contents are associated with the core of the grain, occurring as oscillatory zonations (Fig. 10F*). Less-pronounced Co variations are also visible at the margin of the grain and surrounding the grain core (Fig. 10F and F*). Copper is enriched only in the outer margin of the grain, forming a sharp rim that shows no correlation with Co content (Fig. 10G). Arsenic is homogenously distributed (Fig. 10H). A Co-rich core region is visible in grain 65R1-B (Fig. 10I). The interior of the Co-rich core is characterized by elevated As and Cu contents (Fig. 10J and K). Cobalt in sample 65R1-C occurs as oscillatory zonations again defining a pronounced grain core (Fig. 10L). Arsenic shows some internal variation but is relatively enriched in the matrix surrounding the pyrite grain (Fig. 10M). Copper forms several discrete chalcopyrite grains (Fig. 10N), whilst Se and Sb appear homogenously distributed (Fig. 10O and P).

Discussion

Controls on the distribution of trace metals in pyrite

Variations in fluid composition occur in response to fluid mixing, phase separation, the reaction of ascending fluid with host rocks and/or the addition of magmatic volatiles during degassing (de Ronde et al., 2011; Keith et al., 2016; Metz and Trefry, 2000). The heterogeneous and, in some cases, zoned distribution of Co, Cu, As and Sb in pyrite at Brothers indicate that the source of metals, or composition of

the hydrothermal fluid changed as the pyrite grains grew. Here, we evaluate different processes related to the evolution of the Brothers magmatic-hydrothermal system and how, or indeed if, these processes are preserved as variations in trace metal content across individual pyrite grains.

Fluid mixing

The stability of metal complexes imposes a strong control on the solubility and precipitation of metals (Pokrovski et al. 2013). At temperatures >250°C and NaCl concentrations of >0.6 M, comparable to hydrothermal fluids sampled at Brothers (Kleint et al. 2019), Co is transported as a $CoCl_4^{2-}$ complex (Liu et al. 2011). Arsenic is principally transported as $As(OH)_3$ in acidic hydrothermal fluids at high-temperatures (>300°C; Heinrich and Eadington 1986; Breuer and Pichler 2013). At temperatures of up to ~350°C and a pH of <10, Sb is transported as $Sb(OH)_3^0$ (Zotov et al. 2003). Copper is primarily transported as a $CuCl_2^-$ complex in hydrothermal fluids, whereas $CuCl^{3-}_4$ may be important in hypersaline brines (Liu and McPhail 2005; Reed and Palandri, 2006; Akinfiev and Zotov 2010; cf. hypersaline brines are found in some Brothers fluid inclusions; de Ronde et al. 2019a). Establishing the dominant metal complexes at Brothers is important as this controls the solubility and precipitation of metals in the hydrothermal fluid and thus can affect the distribution of metals within the hydrothermal system.

Based on the distribution of alteration mineral assemblages below the seafloor, three different sub-surface fluid mixing scenarios are possible at Brothers: i) the mixing of low-pH magmatic fluids with ambient (~4°C) seawater, ii) the mixing of high-temperature seawater-derived hydrothermal fluids (>300°C) with ambient seawater, and iii) the mixing of high-temperature (~300°C) seawater-derived hydrothermal fluids with high-temperature, low-pH magmatic fluid. The mixing of magmatic fluid/vapor with infiltrating ambient seawater (i) has only been documented at the Upper Cone where seawater infiltrates through the cone walls (Caratori-Tontini et al. 2012) causing magmatic vapors to condense. This is consistent with vent fluid pH values to 1.8 and the predominance of native sulfur at this site (de Ronde et al. 2011; Kleint et al. 2019; Stucker et al. 2022). At the NW Caldera site, mixing between a hot seawater-derived hydrothermal fluid and magmatic fluid (ii) occurs in deep zones (>189 mbsf) and the mixing of seawater-derived

hydrothermal fluids with ambient seawater (iii) seems to be limited to within ~30 m of the seafloor (de Ronde et al. 2019a).

In sample 23R1 from the Upper Cone, oscillatory zonations in Cu and Sb occur (Fig. 8). This likely results from the localized interaction of magmatic volatile-rich fluid and vapor with infiltrating seawater, as a magmatic volatile source for Cu and Sb has previously been suggested (see magmatic volatile influx; Wohlgemuth-Ueberwasser et al. 2015; Keith et al. 2018; Brandl et al., 2023). However, the general lack of zonation in etched pyrite at the Upper Cone is a consequence of the limited capacity of low-salinity magmatic vapors and fluids to transport metals (Gruen et al. 2014), hence also explaining the absence of massive sulfide mineralization at the seafloor at the Upper Cone (de Ronde et al., 2005).

In near seafloor samples from the NW Caldera site, core section 1R1 (0.1 mbsf) and 5R1 (25.9 mbsf), zonations in As, Sb and to a lesser extent Cu are present (Fig. 9). These zonations formed in response to pronounced and transient fluctuations in fluid temperature and pH that occur during mixing between shallow infiltrating seawater and seawater-derived hydrothermal fluid (~300°C). This is in good agreement with previous studies that showed pyrite in this area contains elevated As and Sb contents (median: 2844 and 25 ppm, respectively, *n=14*; Martin et al. 2022a), and a variable Cu content, ranging from 78 ppm to 630 ppm (Martin et al., 2022a). However, previous studies did not identify discrete zonations in As and Sb content such as those visible in sample1R1 and 5R1 (Fig. 9A and F), that indicate temporal variations in enrichment processes. At the seafloor to a depth of ~30 mbsf, seawater is expected to be near ambient temperature (i.e., a few °C) with a slightly higher pH (~7-8). Hence, sharp zonations in metals that are mobile in intermediate temperature fluids (<300°C), such as As and Sb (Trefry et al. 1994; Metz and Trefry 2000), occur in response to seawater mixing that decrease fluid temperature and increase pH.

In pyrite from deeper pyrophyllite-rich samples (>189 mbsf), specifically core section 65R1, located at a depth of 314 mbsf, zonations in Co content are a common feature (e.g., Fig. 10F, I and L). The Co enrichment pattern is distinct, occurring in the core of the pyrite grains as well-defined oscillatory zonations

(65R1; Fig. 10F, I and L). In seafloor hydrothermal deposits, Co is typically enriched in high-temperature zones (e.g., stockwork; Keith et al. 2016; Monecke et al. 2016; Grant et al. 2018). Experimental studies show that Co is precipitated by a decrease in temperature; a decrease from 300 to 200°C will decrease the solubility of Co by two-orders-of-magnitude (Migdisov et al. 2011).

Unlike samples located in close proximity to the seafloor, at deep crustal levels (i.e., >189 mbsf), sharp and transient changes in the temperature and pH of the hydrothermal fluid are unlikely to occur. Seawater recharge will become progressively heated and acidic due to conductive heating, mixing with ascending magmatic fluid and during chemical exchange with wall rocks, forming a high-temperature (>300°C) seawater-derived hydrothermal fluid (de Ronde et al. 2019a). Therefore, changes in fluid temperature and pH during mixing between magmatic fluids and seawater-derived hydrothermal fluid is unlikely to facilitate Co precipitation at this depth and other processes need to be invoked.

Fluid inclusions analyzed at a depth of 309 mbsf (core section 64R1) at the NW Caldera site are hypersaline (i.e., up to ~43.7 wt.% NaCl equivalent; de Ronde et al. 2019a, b), which indicate the direct exsolution of a volatile-rich brine from the underlying magma. These brines may have contained considerable amounts of Co, as $CoCl_4^{2-}$ complexes are stable in high-salinity fluids (Liu et al. 2011). The dilution of such brines during mixing with seawater-derived hydrothermal fluids (~3.5 wt.% NaCl) may have led to the precipitation of Co-enriched pyrite in core section 65R1 at a depth of 314 mbsf. The fact that similar Co-rich cores are absent in pyrite from core section 55R1 (Fig. 10A), located at 266 mbsf, indicates that brine dilution occurred over a spatially restricted depth interval at around 314 mbsf. The enrichment of Co in early pyrite cores is consistent with the transient nature of brines at the NW Caldera site, with Co becoming progressively depleted toward the margin of the grain due to continued dilution and metal mobilization toward the seafloor (de Ronde et al. 2019a; Gruen et al. 2012).

Magmatic volatile influx

Temporal variations in temperature, salinity, H_2S, SO_2, and CO_2 content of vent fluid have been observed in hydrothermal systems that are thought to occur in response to the intrusion of magma at depth in oceanic crust (Butterfield and Massoth 1994; Von Damm et al. 1995; Butterfield et al. 2011; Von Damm, 2013). This is prominent on the vent site scale with pyrite from the Upper Cone and pyrophyllite-rich alteration at the NW Caldera being enriched in Te, Se, Cu, Bi, Sb and As (Martin et al. 2022a). However, the nature in which magmatic volatiles and associated metals were introduced in to the hydrothermal system(s) remains poorly characterized.

Magmatic volatile degassing is ongoing at the Upper Cone site and to a lesser extent at the older NW Caldera site (de Ronde et al. 2011). Most pyrite grains at the Upper Cone show no internal variation when etched with NaOCl, indicating that fluid conditions (e.g., pH and temperature) did not fluctuate significantly during pyrite growth, further supporting the presence of vapor-rich, low-salinity fluids that had a limited capacity to transport metals at the immature Cone Site (Gruen et al. 2014; de Ronde et al. 2019a).

In sample 23R1, rare oscillatory zonations in Cu and Sb occur (Fig. 8A and B). Keith et al. (2018) and Gruen et al. (2014) suggest that Cu is contributed to the Brothers hydrothermal system through an aqueous S- and Cl-rich magmatic volatile phase that is extracted from a silicate melt. Consequently, the zonation of Cu in pyrite at the Upper Cone could represent the contribution of magmatic volatiles that occurred in temporally discrete, pulsed events (Stucker et al. 2022; Berkenbosch et al. 2019). Similar processes may be responsible for the enrichment of Sb, as a magmatic volatile source has previously been suggested (Wohlgemuth-Ueberwasser et al. 2015). Thus, the coupled relationship between Cu and Sb is best explained by the pulsed addition of magmatic volatiles at the Upper Cone.

The influence of magmatic volatile degassing is expected to be less-pronounced at the NW Caldera site, especially in pyrite from chlorite-rich alteration that overprints older magmatic-volatile alteration (de Ronde et al. 2019a, c). In pyrophyllite-illite samples, only Co consistently exhibits clear oscillatory

zonations, however, there is no evidence to suggest a link between Co-enrichment and magmatic volatile degassing here (Keith et al. 2016; Berkenbosch et al. 2019).

Temporal variations in the source of sulfur at Brothers volcano

Upon mixing and cooling with hydrothermal fluid below ~400°C, SO_2 that is degassed from the magma undergoes disproportionation, producing both SO_4^{2-} and H_2S (Giggenbach 1987). During disproportionation, SO_4^{2-} becomes enriched whilst H_2S is depleted in ^{34}S relative to the starting SO_2 isotopic composition. The amount of fractionation between sulfur species is dependent on temperature and the relative amount of reduced and oxidized sulfur species produced (Kusakabe et al. 2000; McDermott et al. 2015). The disproportionation of SO_2 results in the formation of sulfide minerals with low $\delta^{34}S$ values (often <0‰), for example Hine Hina on the Valu Fa Ridge, Lau back-arc basin (Herzig et al. 1998). Sub-seafloor pyrite at Brothers volcano have similarly low $\delta^{34}S$ values that range from -13.2 to 4.6‰ (Martin et al. 2022a). Chalcopyrite, sphalerite and pyrite in sulfide chimneys at the NW Caldera have a narrower range in $\delta^{34}S$ values, ranging from -5.7 to -0.6‰, indicating that all sulfide minerals precipitated under similar physical and chemical conditions (de Ronde et al. 2011). The $\delta^{34}S$ composition of vent fluid HS^- at the NW Caldera is -1.1 ± 0.7‰ (1σ, *n=6*) and -3.6 ± 2.1‰ (1σ, *n=4*) at the Upper Cone (de Ronde et al. 2003). Here, we examine changes in the source of sulfur recorded as variations in $\delta^{34}S$ values across individual mineral grains.

Magmatic sulfur signature

The average $\delta^{34}S$ value of magmatic sulfides at Brothers is 0.9±2.4‰ *(n=15*, 1σ). This average value is close to the $\delta^{34}S$ range of sulfide in mantle rocks (1.3±3.8‰), mid-ocean ridge (-0.3±2.3‰) and ocean island basalts (1.2±5.6‰) as well as the whole-rock composition of primitive arc rocks (1.0±3.2‰; Marini et al. 2011). The large range of $\delta^{34}S$ values (-3.0 to 6.7‰) is also typical. Higher $\delta^{34}S$ values are typically observed in arc andesitic (2.6±2.3 ‰), dacitic (2.6 to 12.2 ‰) and rhyodacitic (6.3 to 17.8 ‰) whole rocks (Rye et al. 1984; Mandeville et al. 1998;

Luhr & Logan 2002). These heavier S isotope compositions are resulting from open-system or multi-stage degassing of SO_2 from the oxidized magmas (e.g., Mandeville et al. 1998). The light $\delta^{34}S$ composition of magmatic sulfides in the dacites at Brothers volcano can thus be interpreted as further evidence for the formation of these sulfides (immiscible sulfide segregation) in an undegassed magma reservoir at depth (Brandl et al. 2023). These data provide an important constraint on the isotopic composition of sulfur that is leached form magmatic host rocks and their contained magmatic sulfide minerals during hydrothermal alteration and subsequent formation of hydrothermal sulfide mineralization.

Thermochemical sulfate reduction (TSR) and leaching of sulfur from host rocks

The two-component mixing of seawater sulfate (~21‰; Rees et al. 1978) that undergoes TSR and sulfur leached from arc-related oceanic crust (4.4 ± 2.1‰; Ueda and Sakai 1984) produce sulfide minerals with positive $\delta^{34}S$ values, typically between 0 and 5‰ (e.g., Hannington et al. 2005). The average $\delta^{34}S$ value of sulfide minerals in host rocks at Brothers of 0.9 ± 2.4‰ ($n=15$, 1σ) lies within error of values for arc rocks obtained by Ueda and Sakai (1984). Only samples from the NW Caldera site contain $\delta^{34}S$ values that are comparable to arc-related magmatic host rocks ($\delta^{34}S$ >0‰) and therefore could have formed via TSR and leaching of sulfur from host rocks (Fig. 11). In all samples, regardless of depth below the seafloor, the high $\delta^{34}S$ values occur spatially associated with low values that are <0‰ indicating that the source of sulfur, fluid temperature or oxidation state of the fluid changed during pyrite growth.

Previous studies suggest that $\delta^{34}S$ values in sulfide minerals that are >0‰ formed via TSR during seawater entrainment just below the seafloor, or within the chimney structure itself (Janecky and Shanks, 1988). Samples from core section 1R1 and 5R1 contain chlorite, indicating formation temperatures in excess of ~250°C and thus above the lower temperature limit for TSR (160°C; Machel et al. 1995). Therefore, near-seafloor samples with high $\delta^{34}S$ values >0‰ are consistent with sulfur that is contributed by TSR of seawater and the leaching of igneous host rocks, as previously suggested by de Ronde et al. (2005). The

occurrence of low $\delta^{34}S$ values (down to -4.6‰) in the same samples (Fig. 6A-1) indicate periods where a relatively larger proportion of sulfur was sourced from SO_2 disproportionation. These periods are discrete, and interspersed with periods where further sulfur was contributed from TSR and the leaching of host rocks, causing excursions from relatively low to high $\delta^{34}S$ values across the pyrite grains.

In pyrite from deeper pyrophyllite + illite samples from the NW Caldera site (e.g., 65R1, 314 mbsf), there is limited evidence of interactions between seawater-derived hydrothermal fluids and volcanic host rocks as chlorite is absent here (Martin et al. 2022b). Yet pyrite grains analyzed from sample 65R1 still contain high $\delta^{34}S$ values (>0‰) that are comparable to those located near the seafloor. High $\delta^{34}S$ values in deeper samples that are within the range of volcanic host rocks at Brothers (up to 6.7‰; Table 1) and could be explained by the addition of ^{34}S from the leaching of the volcanic host rocks. The fractionation between H_2S and pyrite at temperatures of between 300-400°C is <0.4‰ (Ueda and Sakai, 1984); therefore, it is plausible that leaching of sulfur from the host rocks could explain high $\delta^{34}S$ values of ≤4‰. However, to produce these high values, a closed system where sulfur is only contributed from the leaching of host rocks is needed, and given the abundance of chlorite in samples from below the seafloor at the NW Caldera, indicating the presence of seawater-derived hydrothermal fluids, we suggests that the system was open with respect to seawater influx, as shown in other seafloor hydrothermal systems (e.g., Ono et al. 2007), making a close system scenario unlikely.

SO_2 Disproportionation

In this study, all $\delta^{34}S$ analyses of samples from from the Upper Cone and NW Caldera sites plot below, or within error (max 4.6‰), of the suggested sulfur isotopic composition of Brothers lavas (average 0.9±2.4, *n=15*, 1σ, max 6.7‰). In concert with previous studies, we attribute $\delta^{34}S$ values of <4‰ to sulfur that is contributed from the disproportionation of degassing SO_2, in addition to local TSR and leaching of host rocks. However, unlike previous studies that focused on mineral separates, we show that notable variations in $\delta^{34}S$ values occur across individual pyrite grains, ranging from -4.2 to -8.1 at the Upper Cone site (core section 49R2) and from -1.0 to -8.9 (core section 55R1) from the NW Caldera site. These ranges could

relate to either changes in the temperature or redox conditions of the fluid during SO_2 disproportionation (McDermott et al. 2015), or changes in the relative amounts of sulfur sourced from TSR, leaching of volcanic host rocks, and/or SO_2 disproportionation. Further, multiple sulfur isotopes are needed to discriminate between these processes.

Phase separation

Phase separation can lead to the fractionation of sulfur isotopes due to changes in the oxidation state of the fluid caused by the loss of aqueous H_2S and H_2 to the vapor phase (Drummond and Ohmoto 1985; Palin and Xu, 2000; Hutchison et al. 2020). Evidence from the study of subaerial epithermal and mesothermal Au deposits indicate that oxidation of the hydrothermal fluid during boiling will lead to the preferential partitioning of ^{34}S into SO_2 or SO_4^{2-} producing ^{34}S depleted pyrite (Ohmoto and Lasaga 1982; McKibben and Eldridge 1990; Peterson and Mavrogenes 2014). The NaCl content of vent fluids at Brothers varies from 0.1% to 9.8% NaCl indicating that phase separation of the hydrothermal fluid is occurring (Diehl et al. 2020; Lee et al. 2022). This is supported by fluid inclusion analysis from sub-seafloor drill core samples that have a variable salinity from 2.8% to 43.7 wt.% NaCl (Gruen et al. 2012, 2014; de Ronde et al. 2019a, b, c; Diehl et al. 2020; Lee et al. 2022).

At the Upper Cone, $\delta^{34}S$ values of <4‰ occur in core section 23R1 and 49R2 (Fig. 11). The measured $\delta^{34}S$ of vent fluid HS^- at the Upper Cone is -3.6 ± 2.1‰ (de Ronde et al. 2011). Therefore, pyrite precipitated during boiling that formed from the condensation of an H_2S-rich vapor should contain $\delta^{34}S$ values less than approximately -3.6‰. However, fluid boiling is not the only process that can fractionate sulfur isotopes, as SO_2 disproportionation, which is known to occur widely at Brothers also produces comparably low $\delta^{34}S$ values.

In addition to containing low $\delta^{34}S$ values, pyrite that formed during phase separation is texturally distinct compared to pyrite formed from non-boiling fluids, due to rapid crystallization that forms colloform, inclusion-rich or highly porous pyrite with poorly formed crystal faces (Román et al. 2019). Colloform pyrite occurs in black smoker chimneys at the NW Caldera (de Ronde et al. 2003; 2005; Berkenbosch et al.

2019), but is absent below the seafloor. In pyrite from core section 49R2, an inclusion-rich zone near the core of the grain shows lower $\delta^{34}S$ values (down to -8.1‰ compared to the median for the grain of -5.9‰; Fig. 5B-1). However, variations in fluid temperature during SO_2 disproportionation could also produce these signatures. Thus, it is not possible to distinguish between pyrite that formed during phase separation and pyrite produced during SO_2 disproportionation with the available data.

Temporal variation in the source of metals and sulfur in Brothers volcano

Variations in trace metal content and sulfur isotope ratios across pyrite grains at Brothers volcano are considered to be produced by; i) source variation (e.g., magmatic volatile influx) and for sulfur isotopes, sulfur contributed from TSR and leaching of igneous rocks or, ii) variations in temperature, pH, salinity or redox of the hydrothermal fluid. These variables are linked, as the intrusion of new magma at depth in oceanic crust can change the chemical composition of the hydrothermal fluid, increase fluid temperature and provide a renewed source of some metals to the hydrothermal system (e.g., Butterfield and Massoth 1994). The intrusion of magma occurs as pulsed events (Fox et al. 1995; Johnson et al. 2000; Lilley et al. 2003; Von Damm 2013). Thus, renewed magmatism will directly affect fluid chemistry and key ligand contents (H_2S and Cl) that in turn effect the solubility of metals and the source of sulfur that are preserved as variations in trace metal content and sulfur isotope ratios across individual pyrite grains.

At the Upper Cone site, pyrite rarely shows any internal zonation when etched with NaOCl when compared to pyrite grains analyzed at the NW Caldera site. The lack of internal variation in sample 49R2 suggests that the physical and chemical conditions during pyrite formation did not vary significantly, and that low salinity vapors do not carry significant amounts of metal. The lack of internal variation is supported by an absence of $\delta^{34}S$ values >4‰ that might suggest TSR of seawater, indicating magmatic degassing and SO_2 disproportionation is the major source of sulfur and that sulfur derived from TSR of seawater is a minor component in the sample analyzed. In sample 23R1, a pyrite grain that does show rare internal zonation, the coupled enrichment of Cu and Sb along crystal growth zones is interpreted to represent a new pulse of magmatic volatile-rich fluid (Fig. 12).

Near the seafloor at the NW Caldera site (core sections 1R1 and 5R1), pyrite grains show zones of high As content that correlate with $\delta^{34}S$ values that are >0‰ (up to 3.4‰; Fig. 6 B and C). This confirms that As incorporation into pyrite is related to increased amounts of seawater mixing, and is not associated with either phase separation, or the influx of magmatic volatiles at the NW Caldera site, as these processes would produce pyrite with low $\delta^{34}S$ values. The coupled relationship between As and Sb, directly below the seafloor in core section 1R1 and high $\delta^{34}S$ values are produced during TSR in the shallow subsurface (Fig. 12). Precipitation of As and Sb-rich pyrite occurs in response to decreasing fluid temperature and increasing fluid pH and fO_2 generated by periods of increased seawater influx, most likely relating to permeability increases during faulting events (de Ronde et al. 2005; Caratori Tontini et al. 2012; 2019).

In pyrite samples collected deeper down the borehole at the NW Caldera site (83R1; 400.3 mbsf), but still associated with chlorite-rich alteration, high $\delta^{34}S$ values and oscillatory growth zonations are absent, or less clearly defined relative to the shallow samples (<31 mbsf). The lack of zonation supports previous studies that indicate pyrite has been overprinted by late-stage fluids and undergone recrystallization (Martin et al. 2022a). The absence of high (>4‰) $\delta^{34}S$ values in deeper sourced pyrite (e.g., core section 83R1; 400.3 mbsf) from chlorite-rich alteration indicates; 1) increasing amounts of sulfur obtained from SO_2 disproportionation, 2) the leaching of host rocks, and/or 3) lesser amounts of TSR, when compared with shallow sourced pyrite samples (Fig. 12). At a depth of ~400 mbsf, seawater recharge will have become heated to high-temperatures (>300°C) and have a low-pH relative to its initial composition at, or near the seafloor. Thus, the absence of sharp changes in temperature and pH of the hydrothermal fluid that occur near the seafloor is in stark contrast to conditions deeper down, explaining the lack of internal zonation in trace metals and sulfur isotope ratios in pyrite from deeper chlorite-rich samples (Fig. 6 A vs. D).

Pyrite from pyrophyllite + illite alteration contains $\delta^{34}S$ values that range from -6.9 to 4.6‰, a notably larger range than for other samples analyzed in this study. The enrichment of Co correlates with sharp excursions from relatively low (<0‰) to high $\delta^{34}S$ (>0‰) values in all grains analyzed (Fig. 7, 10F* and 11). This relationship is best preserved in the core of grain 65R1-A and corresponds to an increase in $\delta^{34}S$

values from -2.1 to 4.1‰ (Fig. 7C-3). We discount the contribution of Co from magmatic volatile degassing that is commonly also associated with the disproportionation of SO_2, as high Co concentrations do not correlate with decreasing $\delta^{34}S$ values. Instead, we interpret Co-rich zones as representing a period of brine dilution where seawater-derived hydrothermal fluids interacted with magmatic brines that were exsolved directly from volatile-saturated magmas at Brothers (Fig. 12) (Gruen et al. 2014; de Ronde et al. 2011; 2019). The interaction of brines with seawater-derived hydrothermal fluid decreased fluid salinity causing the destabilization of $CoCl_4^{2-}$ complexes and introduced ^{34}S enriched sulfur derived from TSR of seawater in an environment otherwise dominated by sulfur sourced from SO_2 disproportionation. Studies show a decrease in NaCl content from 5 to 0.1 M at 300°C will cause a decrease in fluid Co concentration from 142 to 0.6 ppm, precipitating Co-rich pyrite (Liu et al. 2011). A decrease in Co solubility could also occur by decreasing temperature. However, sample 65R1 is located at a depth of ~314 mbsf and at this depth a significant decrease in fluid temperature (<100°C) or pH is unlikely to occur. The sulfur isotopic variation across pyrite grains in sample 65R1 (Hole U1530A; NW Caldera) support the ingress of sulfur from seawater-derived hydrothermal fluid where TSR produces $\delta^{34}S$ values >0‰ and up to 4.6‰ (Fig. 12). This dilution event could conceivably relate to the initial ingress of seawater deep below the seafloor at Brothers during the initial development of ring fault systems during caldera formation, preserving the transition from a magmatic volatile-dominated to seawater-influenced hydrothermal system (de Ronde et al. 2019a).

The distribution of Cu in pyrite from sample 65R1 does not correlate with Co (Fig. 10F and G). The lack of correlation between Co and Cu is unexpected, as both elements are transported as Cl^- complexes and can occur at high-concentrations in saline brines, and would both be deposited during fluid mixing between brine and seawater-derived hydrothermal fluids (Liu et al. 2011; Liu and McPhail, 2005). The absence of any correlation between Co in Cu is attributed to the mineral-scale partitioning of Cu at Brothers. That is, Cu is preferentially enriched in chalcopyrite (Fig. 10N), depleting co-precipitated pyrite in Cu. By contrast, Co is readily incorporated into pyrite and does not commonly form its own mineral phase (e.g., Co-pentlandite; Marques et al. 2007) and hence is unaffected by the formation of chalcopyrite.

Implications for understanding ore deposit formation

The significance of brines and magmatic volatile influx as a source of metals in ore forming systems, such as porphyry Cu deposits, has long been recognized (Blundy et al. 2021; Reich et al. 2013; Ulrich et al. 1999). Understanding the spatial and temporal distribution of brines is important as they are often enriched in metals that are considered critical for a transition to a low carbon economy, such as Cu and Co (Blundy et al. 2021; Heijlen et al. 2021). In contrast, magmatic volatile influx may be important in the enrichment of metals such as Te, Se, As or Sb (Patten et al. 2020; Keith et al. 2016). Understanding when the addition of brines or magmatic volatile influx occurs is imperative, as this can influence the distribution of metals at the deposit-scale (e.g., Keith et al., 2022). The challenge in many ore forming systems, including SMS deposits, is that early mineralizing events, or events that are temporally discrete, can be overprinted and erased over time by subsequent fluid flow events. This makes linking changes in the source of metals (e.g., brines) to the geochemical signature preserved in sulfide minerals difficult to establish.

At Brothers, we show that temporal variations in brine dilution and magmatic volatile influx can be preserved across individual pyrite grains over their protracted growth histories. Brines, if present occurred early in magmatic-hydrothermal evolution and were later overprinted by seawater-derived hydrothermal fluids. Our data supports the occurrence of magmatic brines below the seafloor and shows that brines acted as a sink for Co. In contrast, magmatic volatile elements such as Se, As and Sb move through the system and are less affected by brine formation. Therefore, targeting early pyrite generations may be beneficial for Co and Cu extraction. Ultimately, the sequestration of brines below the seafloor may be widespread in other SMS deposits and can affect the trace metal signature of sulfide mineralization at the seafloor. Hence, in addition to near surface (~20 m) or seafloor processes such as fluid mixing between seawater and hydrothermal fluid, deeper processes of brine formation (i.e., 315 mbsf) are important in controlling the metal endowment of SMS/VMS deposits.

Summary and conclusions

Data collected in this study highlight the importance of applying mineral-scale geochemical and isotopic ($\delta^{34}S$) data to understand temporal variations in the cycling of sulfur and trace metals in seafloor hydrothermal systems. More variation in the $\delta^{34}S$ composition of pyrite is observed across a single ~1 mm grain, where values range from -5.3‰ to 4.6‰, than was previously reported for all bulk pyrite analyses, allowing temporal variations in the source(s) of sulfur at Brothers to be investigated. At the Upper Cone (Site U1528), pyrite rarely shows internal growth zones and contains uniformly low $\delta^{34}S$ values (<0‰) indicating relatively homogenous fluid conditions during its formation, i.e., from fluids that were metal-poor, low-salinity, and vapor-rich with a low potential to transport significant quantities of metals. Where internal zonations do exist, a coupled relationship between Cu and Sb is observed with corresponding low $\delta^{34}S$ values, which we attribute to pulsed magmatic volatile degassing and SO_2 disproportionation.

At the NW Caldera (Site U1530), near seafloor pyrite sampled from chlorite-rich alteration (<31 mbsf) shows multiple generations of overgrowths with obvious internal zonations. Arsenic, which is commonly enriched in low-temperature sulfide mineral assemblages (Grant et al. 2018), is enriched in pyrite due to mixing between seawater and hydrothermal fluids that fluctuated in response to permeability changes in the shallow subsurface. In pyrite recovered from deeper (~400 mbsf) chlorite-rich samples, relatively high $\delta^{34}S$ values are not recorded, indicating increasing amounts of sulfur from SO_2 disproportionation with depth below the seafloor.

Pyrite grains from pyrophyllite-rich alteration at the NW Caldera site have the most variable $\delta^{34}S$ values ranging from -6.9‰ to 4.6‰. Pyrite grains are anhedral and highly resorbed with Co enrichment in relict grain cores. Zones of high Co content correspond to shifts in $\delta^{34}S$ values from >0‰ to <0‰. We attribute this relationship to the ingress of a seawater-derived hydrothermal fluid deep below the seafloor, perhaps related to the initial phase of caldera collapse and seawater ingress that caused the dilution of the magmatic brines at Brothers, which reduced the salinity of the brine resulting in the precipitation of Co-rich pyrite. Our data further highlights the critical role of seawater-derived hydrothermal fluids in metal remobilization

(cf. de Ronde et al. 2019a) and provides evidence of brine dilution deep below the seafloor at the NW Caldera.

When coupled with sulfur isotope analysis, the distribution of trace metals in pyrite can be used to distinguish temporal variations in metal sources and chemical changes in the hydrothermal fluid composition at Brothers that varies both with depth below the seafloor, and spatially between the Upper Cone and NW Caldera sites. We provide evidence supporting the transient nature of brines in seafloor hydrothermal systems, and show that brine formation can sequester Co below the seafloor affecting the chemical composition of sulfide mineralization at higher levels in the magmatic-hydrothermal system and ultimately the seafloor.

Acknowledgments

This research used samples provided by the International Ocean Discovery Program (IODP). We thank the crew and technical staff aboard the D/V *JOIDES Resolution* during Expedition 376: “Brothers Arc Flux”, May-July 5th, 2018. CdR acknowledges funding from the Ministry of Business, Innovation and Employment (MBIE) of the New Zealand Government by way of a GNS SSIF (Strategic Science Investment Fund) award. JWJ acknowledges the support of the Canadian Research Chair program. W Aylward is thanked for assistance whilst performing EPMA mapping. We thank V Maslennikov and an anonymous reviewer for their constructive comments and Editor-in-Chief K Kelley for the editorial handling of this manuscript.

Author Contribution

AJM was responsible for the study conception and design. Material preparation, data collection and analysis was performed by AJM, GP and WA. The manuscript was written by AJM, and all authors provided comments on previous versions of the manuscript. All authors read and approved the final manuscript.

Statements and Decelerations

Conflict of Interest: The authors declare no competing interests.

References

Akinfiev NN, Zotov AV (2010) Thermodynamic description of aqueous species in the system Cu-Ag-Au-S-O-H at temperatures of 0–600°C and pressures of 1–3000 bar. Geochem Int 48:714–720

Baker ET (1998) Patterns of event and chronic hydrothermal venting following a magmatic intrusion: new perspectives from the 1996 Gorda Ridge eruption. Deep Sea Res Part II: Top Stud Oceanogr 45:2599–2618

Baker ET (1995) Characteristics of hydrothermal discharge following a magmatic intrusion. Geol Soc Spec Pub 87:65–76

Baker ET, Walker SL, Embley RW, de Ronde CEJ (2012) High-Resolution Hydrothermal Mapping of Brothers Caldera, Kermadec Arc. Econ Geol 107(8):1583–1593

Berkenbosch HA, de Ronde CEJ, Ryan CG, McNeill AW, Howard DL, Gemmell JB, Danyushevsky LV (2019) Trace Element Mapping of Copper- and Zinc-Rich Black Smoker Chimneys from Brothers Volcano, Kermadec Arc, Using Synchrotron Radiation XFM and LA-ICP-MS. Econ Geol 114:67–92

Berkenbosch HA, de Ronde CEJ, Gemmell JB, McNeill AW, Goemann K (2012) Mineralogy and Formation of Black Smoker Chimneys from Brothers Submarine Volcano, Kermadec Arc. Econ Geol 107:1613–1633

Bischoff JL, Rosenbauer RJ (1984) The critical point and two-phase boundary of seawater, 200– 500°C. Earth Planet Sci Lett 68:172–180

Blundy J, Afanasyev A, Tattitch B, Sparks S, Melnik O, Utkin I, Rust A (2021) The economic potential of metalliferous sub-volcanic brines. R Soc Open Sci 8:202192

Brandl PA, Portnyagin M, Zeppenfeld H, Tepley III FJ, Timm C, Hauff F, Garbe-Schönberg D, Bousquet R (2023) The Origin of Magmas and Metals at the Submarine Brothers Volcano, Kermadec Arc, New Zealand. Econ Geol https://doi.org/10.5382/econgeo.4973

Breuer C, Pichler T (2013) Arsenic in marine hydrothermal fluids: Source, fate and environmental implications. Chem Geol 348:2–14

Brueckner SM, Piercey SJ, Layne GD, Piercey G, Sylvester PJ (2015) Variations of sulphur isotope signatures in sulphides from the metamorphosed Ming Cu(−Au) volcanogenic massive sulphide deposit, Newfoundland Appalachians, Canada. Miner Deposita 50:619–640

Butler IB, Nesbitt RW (1999) Trace element distributions in the chalcopyrite wall of a black smoker chimney: insights from laser ablation inductively coupled plasma mass spectrometry (LA–ICP–MS). Earth Planet Sci Lett 167:335–345

Butterfield DA, Massoth GJ (1994) Geochemistry of north Cleft segment vent fluids: Temporal changes in chlorinity and their possible relation to recent volcanism. J Geophys Res Solid Earth 99: 4951–4968.

Butterfield DA, Nakamura K, Takano B, Lilley MD, Lupton JE, Resing JA, Roe KK (2011) High SO2 flux, sulfur accumulation, and gas fractionation at an erupting submarine volcano. Geology 39:803–806

Caratori Tontini F, Tivey MA, de Ronde CEJ, Humphris SE (2019) Heat Flow and Near-Seafloor Magnetic Anomalies Highlight Hydrothermal Circulation at Brothers Volcano Caldera, Southern Kermadec Arc, New Zealand. Geophys Res Lett 46:8252–8260

Caratori Tontini F, de Ronde CEJ, Yoerger D, Kinsey J, Tivey M (2012) 3-D focused inversion of near-seafloor magnetic data with application to the Brothers volcano hydrothermal system, Southern Pacific Ocean, New Zealand. J Geophys Res Solid Earth 117:B10102

Cox SF (1987) Flow mechanisms in sulphide minerals. Ore Geol Rev 2:133–171

Cox SF, Etheridge MA, Hobbs BE (1981) The experimental ductile deformation of polycrystalline and single crystal pyrite. Econ Geol 76:2105–2117

de Ronde CEJ, Faure K, Bray CJ, Chappell DA, Wright IC (2003) Hydrothermal fluids associated with seafloor mineralization at two southern Kermadec arc volcanoes, offshore New Zealand. Miner Deposita 38:217–233

de Ronde CEJ, Massoth GJ, Butterfield DA, Christenson BW, Ishibashi J, Ditchburn RG, Hannington MD, Brathwaite RL, Lupton JE, Kamenetsky VS, Graham IJ, Zellmer GF, Dziak RP, Embley RW, Dekov VM, Munnik F, Lahr J, Evans LJ, TakaI K (2011) Submarine hydrothermal activity and gold-rich mineralization at Brothers Volcano, Kermadec Arc, New Zealand. Miner Deposita 46:541–584

de Ronde CEJ, Hannington MD, Stoffers P, Wright IC, Ditchburn RG, Reyes AG, Baker ET, Massoth GJ, Lupton JE, Walker SL, Greene RR, Soong CWR, Ishibashi J, Lebon GT, Bray CJ, Resing JA (2005) Evolution of a Submarine Magmatic-Hydrothermal System: Brothers Volcano, Southern Kermadec Arc, New Zealand. Econ Geol 100:1097–1133

de Ronde CEJ, Humphris SE, Höfig TW, Reyes AG and the Expedition 376 Science Party (2019a) Critical role of caldera collapse in the formation of seafloor mineralization: The case of Brothers volcano. Geology 47:762–766

de Ronde CEJ, Humphris SE, Höfig TW, and the Expedition 376 Scientists (2019b) Site U1528, Proceedings of the International Ocean Discovery Program 376, College Station, TX (International Ocean Discovery Program), p. 267.

de Ronde CEJ, Humphris SE, Höfig TW, and the Expedition 376 Scientists (2019c) Site U1530, Proceedings of the International Ocean Discovery Program 376, College Station, TX (International Ocean Discovery Program), p. 267.

Diehl A, de Ronde CEJ, Bach W (2020) Subcritical Phase Separation and Occurrence of Deep-Seated Brines at the NW Caldera Vent Field, Brothers Volcano: Evidence from Fluid Inclusions in Hydrothermal Precipitates. Geofluids 2020:8868259

Drummond SE, Ohmoto H (1985) Chemical evolution and mineral deposition in boiling hydrothermal systems. Econ Geol 80:126–147

Embley RW, de Ronde CEJ, Merle SG, Davy B, Tontini FC (2012) Detailed Morphology and Structure of an Active Submarine Arc Caldera: Brothers Volcano, Kermadec Arc. Econ Geol 107:1557–1570

Fallick AE, Boyce AJ, McConville P (2012) Sulphur stable isotope systematics in diagenetic pyrite from the North Sea hydrocarbon reservoirs revealed by laser combustion analysis. Isot Environ Health Stud 48:144–165

Fox CG, Radford WE, Dziak RP, Lau T-K, Matsumoto H, Schreiner AE (1995) Acoustic detection of a seafloor spreading episode on the Juan de Fuca Ridge using military hydrophone ` arrays. Geophys Res Lett 22:131–134

Fuchs S, Hannington MD, Petersen S (2019) Divining gold in seafloor polymetallic massive sulfide systems. Miner Deposita 54:789–820

Gemmell JB, Sharpe R, Jonasson IR, Herzig PM (2004) Sulfur Isotope Evidence for Magmatic Contributions to Submarine and Subaerial Gold Mineralization: Conical Seamount and the Ladolam Gold Deposit, Papua New Guinea. Econ Geol 99:1711–1725

Giggenbach WF (1987) Redox processes governing the chemistry of fumarolic gas discharges from White Island, New Zealand. Appl Geochemistry 2:143–161

Grant HLJ, Hannington MD, Petersen S, Frische M, Fuchs SH (2018) Constraints on the behavior of trace elements in the actively-forming TAG deposit, Mid-Atlantic Ridge, based on LA-ICP-MS analyses of pyrite. Chem Geol 498:45–71

Gruen G, Weis P, Driesner T, Heinrich CA, de Ronde CEJ (2014) Hydrodynamic modeling of magmatic–hydrothermal activity at submarine arc volcanoes, with implications for ore formation. Earth Planet Sci Lett 404:307–318

Gruen G, Weis P, Driesner T, de Ronde CEJ, Heinrich CA (2012) Fluid-Flow Patterns at Brothers Volcano, Southern Kermadec Arc: Insights from Geologically Constrained Numerical Simulations. Econ Geol 107:1595–1611

Haase KM, Stroncik N, Garbe-Schönberg D, Stoffers P (2006) Formation of island arc dacite magmas by extreme crystal fractionation: An example from Brothers Seamount, Kermadec island arc (SW Pacific). J Volcanol Geotherm Res 152, 316-330

Hannington MD, de Ronde CEJ, Petersen S (2005) Sea-floor tectonics and submarine hydrothermal systems. In: Economic Geology 100th Anniversary Volume. Hedenquist, JW, Thompson, JFH, Goldfarb RJ, Richards JP (ed.). Society of Economic Geologists, Littelton, Colorado, USA, pp. 111–141.

Hedenquist JW, Aoki M, Shinohara H (1994) Flux of volatiles and ore-forming metals from the magmatic-hydrothermal system of Satsuma Iwojima volcano. Geology 22:585–588

Hedenquist JW, Lowenstern JB (1994) The role of magmas in the formation of hydrothermal ore deposits. Nature 370:519–527

Heijlen W, Franceschi G, Duhayon C, Van Nijen K (2021) Assessing the adequacy of the global land-based mine development pipeline in the light of future high-demand scenarios: The case of the battery-metals nickel (Ni) and cobalt (Co). Resour Policy 73:102202

Heinrich CA, Eadington PJ (1986) Thermodynamic predictions of the hydrothermal chemistry of arsenic, and their significance for the paragenetic sequence of some cassiterite-arsenopyrite-base metal sulfide deposits. Econ Geol 81:511–529

Herzig PM, Hannington MD (1995) Polymetallic massive sulfides at the modern seafloor a review. Ore Geol Rev 10:95–115

Herzig PM, Hannington MD, Arribas A (1998) Sulfur isotopic composition of hydrothermal precipitates from the Lau back-arc: implications for magmatic contributions to seafloor hydrothermal systems. Miner Deposita 33:226–237

Huston DL, Sie SH, Suter GF, Cooke DR, Both RA (1995) Trace elements in sulfide minerals from eastern Australian volcanic-hosted massive sulfide deposits; Part I, Proton microprobe analyses of pyrite, chalcopyrite, and sphalerite, and Part II, Selenium levels in pyrite; comparison with delta 34 S values and implications for the source of sulfur in volcanogenic hydrothermal systems. Econ Geol 90:1167–1196

Hutchison W, Finch AA, Boyce AJ (2020) The sulfur isotope evolution of magmatic-hydrothermal fluids: insights into ore-forming processes. Geochim Cosmochim Acta 288:176–198

Janecky DR, Shanks WC (1988) Computational modeling of chemical and sulfur isotopic reaction processes in seafloor hydrothermal systems: chimneys, massive sulfides, and subjacent alteration zones. Canad Mineral 26:805–825

Johnson HP, Hutnak M, Dziak RP, Fox CG, Urcuyo I, Cowen, JP, Nabelek J, Fisher C (2000) Earthquake-induced changes in a hydrothermal system on the Juan de Fuca mid-ocean ridge. Nature 407:174–177

Keith M, Haase KM, Chivas AR, Klemd R (2022) Phase separation and fluid mixing revealed by trace element signatures in pyrite from porphyry systems. Geochim Cosmochim Acta 329:185–205

Keith M, Haase KM, Klemd R, Smith DJ, Schwarz-Schampera U, Bach W (2018) Constraints on the source of Cu in a submarine magmatic-hydrothermal system, Brothers volcano, Kermadec island arc. Contrib to Mineral Petrol 173:40

Keith M, Häckel F, Haase KM, Schwarz-Schampera U, Klemd R (2016) Trace element systematics of pyrite from submarine hydrothermal vents. Ore Geol Rev 72:728–745

Kleint C, Bach W, Diehl A, Fröhberg N, Garbe-Schönberg D, Hartmann JF, de Ronde CEJ, Sander SG, Strauss H, Stucker VK, Thal J, Zitoun R, Koschinsky A (2019) Geochemical characterization of highly diverse hydrothermal fluids from volcanic vent systems of the Kermadec intraoceanic arc. Chem Geol 528:119289

Kusakabe M, Komoda Y, Takano B, Abiko T (2000) Sulfur isotopic effects in the disproportionation reaction of sulfur dioxide in hydrothermal fluids: implications for the δ34S variations of dissolved bisulfate and elemental sulfur from active crater lakes. J Volcanol Geotherm Res 97:287–307

Lee HY, Seo J-H, de Ronde CEJ, Heinrich CA (2022) Fluid Inclusion Evidence for Subseafloor Magmatic-Hydrothermal Processes at Brothers Volcano, Kermadec Arc, New Zealand. Economic Geology. https://doi.org/10.5382/econgeo.4884

Lilley MD, Butterfield DA, Lupton JE, Olson EJ (2003) Magmatic events can produce rapid changes in hydrothermal vent chemistry. Nature 422:878–881

Liu W, Borg SJ, Testemale D, Etschmann B, Hazemann J-L, Brugger J (2011) Speciation and thermodynamic properties for cobalt chloride complexes in hydrothermal fluids at 35–440°C and 600bar: An in-situ XAS study. Geochim Cosmochim Acta 75:1227–1248

Liu W, McPhail DC (2005) Thermodynamic properties of copper chloride complexes and copper transport in magmatic-hydrothermal solutions. Chem Geol 221:21–39

Luhr JF, Logan MAV (2002) Sulfur isotope systematics of the 1982 El Chichón trachyandesite: an ion microprobe study. Geochim Cosmochim Acta 66:3303–3316

Machel HG, Krouse HR, Sassen R (1995) Products and distinguishing criteria of bacterial and thermochemical sulfate reduction. Appl Geochemistry 10:373–389

Mandeville CW, Sasaki A, Saito G, Faure K, King R, Hauri E (1998) Open-system degassing of sulfur from Krakatau 1883 magma. Earth Planet Sci Lett160:709–722

Marini L, Moretti R, Accornero M (2011) Sulfur Isotopes in Magmatic-Hydrothermal Systems, Melts, and Magmas. Rev Mineral Geochem 73:423–492

Marques AFA, Barriga FJAS, Scott SD (2007) Sulfide mineralization in an ultramafic-rock hosted seafloor hydrothermal system: From serpentinization to the formation of Cu–Zn–(Co)-rich massive sulfides. Mar Geol 245:20–39

Martin AJ, Jamieson JW, de Ronde CEJ, Humphris SE, McDonald I, Layne GD Piercey G, MacLeod CJ (2022a) Trace metal and sulfur cycling in a hydrothermally active arc volcano: deep-sea drilling of the Brotehrs volcano, Kermadec arc, New Zealand. Mineral Deposita https://doi.org/10.1007/s00126-022-01135-x

Martin AJ, Jamieson JW, de Ronde CEJ, Humphris SE, Roberts S, MacLeod CJ, Cai Y, Zhang C, Schlict EM, Nozaki T (2022b). Hydrothermal alteration within the Brothers submarine arc volcano, Kermadec arc, New Zealand. Econ Geol https://doi.org/10.5382/econgeo.4962

Martin AJ, Keith M, Parvaz DB, McDonald I, Boyce AJ, McFall KA, Jenkin GRT, Strauss H, MacLeod CJ (2019) Effects of magmatic volatile influx in mafic VMS hydrothermal systems: evidence from the Troodos ophiolite, Cyprus. Chem Geol 531:119325

Massoth GJ, Butterfield DA, Lupton JE, McDuff RE, Lilley MD, Jonasson IR (1989) Submarine venting of phase-separated hydrothermal fluids at Axial Volcano, Juan de Fuca Ridge. Nature 340:702-705

McDermott JM, Ono S, Tivey MK, Seewald JS, Shanks WC, Solow AR (2015) Identification of sulfur sources and isotopic equilibria in submarine hot-springs using multiple sulfur isotopes. Geochim CosmochimActa 160:169–187

McKibben MA, Eldridge CS (1990) Radical sulfur isotope zonation of pyrite accompanying boiling and epithermal gold deposition; a SHRIMP study of the Valles Caldera, New Mexico. Econ Geol 85:1917–1925

Metz S, Trefry JH (2000) Chemical and mineralogical influences on concentrations of trace metals in hydrothermal fluids. Geochim Cosmochim Acta 64:2267–2279

Migdisov A, Zezin D, Williams-Jones AE (2011) An experimental study of Cobalt (II) complexation in Cl− and H2S-bearing hydrothermal solutions. Geochim et Cosmochim Acta 75:4065–4079

Monecke T, Petersen S, Hannington MD, Grant H, Samson I (2016) The minor element endowment of modern sea-floor massive sulfide deposits and comparison with deposits hosted in ancient volcanic successions. In: Rare Earth and Critical Elements in Ore Deposits. Verplanck PL, Hitzman MW (ed.). Society of Economic Geologists, Knoxville, pp. 245–306.

Ohmoto H, Lasaga AC (1982) Kinetics of reactions between aqueous sulfates and sulfides in hydrothermal systems. Geochim Cosmochim Acta 46:1727–1745

Ono S, Shanks WC, Rouxel OJ, Rumble D (2007) S-33 constraints on the seawater sulfate contribution in modern seafloor hydrothermal vent sulfides. Geochim Cosmochim Acta 71:1170–1182

Palin JM, Xu Y (2000) Gilt by Association? Origins of Pyritic Gold Ores in the Victory Mesothermal Gold Deposit, Western Australia. Econ Geol 95:1627–1634

Patten CGC, Pitcairn IK, Alt JC, Zack T, Lahaye Y, Teagle DAH, Markdahl K (2020) Metal fluxes during magmatic degassing in the oceanic crust: sulfide mineralisation at ODP site 786B, Izu-Bonin forearc. Mineral Deposita 55:469–489

Peterson EC, Mavrogenes JA (2014) Linking high-grade gold mineralization to earthquake-induced fault-valve processes in the Porgera gold deposit, Papua New Guinea. Geology 42:383–386

Pokrovski GS, Borisova AY, Bychkov AY (2013) Speciation and Transport of Metals and Metalloids in Geological Vapors. Rev Mineral Geochem 76:165–218

Reed MH, Palandri J (2006) Sulfide Mineral Precipitation from Hydrothermal Fluids. Rev Mineral Geochem 61:609–631

Rees CE, Jenkins WJ, Monster J (1978) The sulphur isotopic composition of ocean water sulphate. Geochim Cosmochim Acta 42:377–381

Reich M, Deditius A, Chryssoulis S, Li J-W, Ma C-Q, Parada MA, Barra F, Mittermayr F (2013) Pyrite as a record of hydrothermal fluid evolution in a porphyry copper system: A SIMS/EMPA trace element study. Geochim Cosmochim Acta 104:42–62

Román N, Reich M, Leisen M, Morata D, Barra F, Deditius AP (2019) Geochemical and micro-textural fingerprints of boiling in pyrite. Geochim Cosmochim Acta 246:60–85

Rona PA, Hannington MD, Raman CV, Thompson G, Tivey MK, Humphris SE, Lalou C, Petersen S (1993) Active and relict sea-floor hydrothermal mineralization at the TAG hydrothermal field, Mid-Atlantic Ridge. Econ Geol 88:1989-2017

Rye RO, Luhr JF, Wasserman MD (1984) Sulfur and oxygen isotopic systematics of the 1982 eruptions of El Chichón Volcano, Chiapas, Mexico. J Volcanol Geotherm Res 23:109–123

Seyfried WE, Seewald JS, Berndt ME, Ding K, Foustoukos DI (2003) Chemistry of hydrothermal vent fluids from the Main Endeavour Field, northern Juan de Fuca Ridge: Geochemical controls in the aftermath of June 1999 seismic events. J Geophys Res Solid Earth 108:B9

Seyfried WE, Mottl MJ (1982) Hydrothermal alteration of basalt by seawater under seawater-dominated conditions. Geochim Cosmochim Acta 46:985–1002

Stucker VK, de Ronde CEJ, Laurence KJ, Phillips AM (2022) Rare Time Series of Hydrothermal Fluids for a Submarine Volcano: 14 Years of Vent Fluid Compositions for Brothers Volcano, Kermadec Arc New Zealand. Econ Geol https://doi.org/10.5382/econgeo.4922

Tanner D, Henley RW, Mavrogenes JA, Holden P (2016) Sulfur isotope and trace element systematics of zoned pyrite crystals from the El Indio Au–Cu–Ag deposit, Chile. Contrib to Mineral and Petrol 171:33

Timm C, de Ronde CEJ, Leybourne MI, Layton-Matthews D, Graham IJ (2012) Sources of Chalcophile and Siderophile Elements in Kermadec Arc Lavas. Econ Geol 107:1527–1538

Trefry JH, Butterfield D B, Metz S, Massoth GJ, Trocine R P, Feely RA (1994) Trace metals in hydrothermal solutions from Cleft segment on the southern Juan de Fuca Ridge. J Geophys Res Solid Earth 49:4925-4935

Ueda A, Sakai H (1984) Sulfur isotope study of Quaternary volcanic rocks from the Japanese Islands Arc. Geochim et Cosmochim Acta 48:1837–1848.

Ulrich T, Günther D, Heinrich CA (1999) Gold concentrations of magmatic brines and the metal budget of porphyry copper deposits. Nature 399:676–679

Vanko DA, Bach W, Roberts S, Yeats CJ, Scott SD (2004) Fluid inclusion evidence for subsurface phase separation and variable fluid mixing regimes beneath the deep-sea PACMANUS hydrothermal field, Manus Basin back arc rift, Papua New Guinea. J Geophys Res Solid Earth 109:B03201

Von Damm KL (2000) Chemistry of hydrothermal vent fluids from 9°–10°N, East Pacific Rise: “Time zero,” the immediate posteruptive period. J Geophys Res Solid Earth 105:11203–11222

Von Damm KL (2013) Controls on the Chemistry and Temporal Variability of Seafloor Hydrothermal Fluids. In: Seafloor Hydrothermal Systems: Physical, Chemical, Biological, and Geological Interactions, Volume 91, Humphris SE, Zierenberg RA, Mullineaux LS, Thomson RE (ed.). American Geophysical Union, pp. 222–247

Von Damm KL, Oosting SE, Kozlowski R, Buttermore LG, Colodner DC, Edmonds HN, Edmond JM, Grebmeier JM (1995) Evolution of East Pacific Rise hydrothermal vent fluids following a volcanic eruption. Nature 375:47–50

Wang Y, Han X, Petersen S, Frische M, Qiu Z, Cai Y, Zhou P (2018) Trace Metal Distribution in Sulfide Minerals from Ultramafic-Hosted Hydrothermal Systems: Examples from the Kairei Vent Field, Central Indian Ridge. Minerals 8:526

Wohlgemuth-Ueberwasser CC, Viljoen F, Petersen S, Vorster C (2015) Distribution and solubility limits of trace elements in hydrothermal black smoker sulfides: An in-situ LA-ICP-MS study. Geochim Cosmochim Acta 159:16–41

Wysoczanski RJ, Handler MR, Schipper CI, Leybourne MI, Creech J, Rotella MD, Nichols ARL, Wilson CJN, Stewart RB (2012) The Tectonomagmatic Source of Ore Metals and Volatile Elements in the Southern Kermadec Arc. Econ Geol 107:1539–1556

Yang K, Scott SD (1996) Possible contribution of a metal-rich magmatic fluid to a sea-floor hydrothermal system. Nature 383:420–423

Zotov AV, Shikina ND, Akinfiev NN (2003) Thermodynamic properties of the Sb(III) hydroxide complex Sb(OH)3(aq) at hydrothermal conditions. Geochim Cosmochim Acta 67:1821– 1836

Figure Captions

Figure 1: Location of the Brothers volcano. **a** Bathymetric map showing the location of Brothers volcano and surrounding tectonic features associated with the Tonga-Kermadec intra-oceanic arc. **b** Bathymetric map of Brothers caldera showing the location of the NW Caldera site (Site U1530, Hole U1530A) and the Upper Cone site (Site U1528, Hole U1528D). **c** 3D bathymetry showing the location of the NW Caldera and Upper Cone sites (Data: GNS Science) (2 x vertical exaggeration).

Figure 2: Drill core from the Upper Cone site (Site U1528, Hole U1528D). **a** Half core sections showing the location of samples analyzed in this study. **b** Core section 23R1 (162.5 mbsf) has a brecciated texture with clasts appearing dark in color and less altered than the surrounding matrix. The sample contains natroalunite + pyrophyllite + anhydrite + pyrite + quartz and native sulfur. **b1** Photomicrograph in reflected light of fine-grained euhedral pyrite from core section 23R1 that occurs associated with natroalunite and pyrophyllite in the matrix. **c** Core section 49R2 (253.7 mbsf) has a massive texture and contains natroalunite + smectite + anhydrite + pyrite + quartz + cristobalite + native sulfur. **c1** Subhedral coarse-grained pyrite within a vug from sample 49R2. Location of pyrite grains within the drill core samples are shown by the red boxes.

Figure 3: Drill core samples from the NW Caldera site (Site U1530, Hole U1530A). **a** Half core sections showing the location of samples analyzed in this study. **b** Core section 1R1 (0.1 mbsf). Clasts are chlorite + illite-rich with a brecciated texture in a matrix of pyrite + anhydrite + barite with sphalerite. **b1** Photomicrograph in reflected light of pyrite with minor marcasite (Mrc) forming discrete veins in sample 1R1. **c** Core section 5R1 (25.9 mbsf). Chlorite + illite-rich clasts in a matrix of pyrite and anhydrite. **c1** Aggregates of coarse-grained euhedral pyrite associated with anhydrite and quartz from sample 5R1 forming discrete veins. **d** Core section 55R1 (265.9 mbsf). Pyrophyllite + illite + diaspore + rutile + anhydrite + pyrite with a prominent, mottled, equigranular texture. The sample is cut by an anhydrite vein that has a rim of pyrite. **d1** Subhedral to anhedral coarse-grained pyrite from sample 55R1. Pyrite analyzed occurs in the matrix intergrown with pyrophyllite, quartz and anhydrite. **e** Core section 65R1 (313.9 mbsf)

containing pyrophyllite + illite + anhydrite + pyrite with a massive-to-equigranular texture. **e1** Coarse-grained anhedral pyrite from sample 65R1. **f** Core section 83R1 (400.3 mbsf) has a massive texture containing chlorite + quartz + illite + anhydrite with disseminated pyrite. **f1** Aggregate of euhedral pyrite from sample 83R1 associated with chlorite and quartz. The location of pyrite grains within the drill core samples are shown by the red boxes.

Figure 4: Representative pyrite from the Upper Cone (a-c) and NW Caldera (d-f) that has been etched for 90 s using NaOCl. **a** Subhedral pyrite with no internal zonation. **b** Aggregate of fine-grained pyrite with boundaries between different sub-grains visible. **c** Pyrite showing oscillatory zonation with a late overgrowth of fine-grained pyrite. **d** Pyrite with oscillatory zonation that is parallel to the grain margin. **e** Pyrite with oscillatory zonation that is sub-parallel to the grain margin. **f** Subhedral pyrite with random zonation toward the core (inset image: close-up of zonation).

Figure 5: Pyrite grains from the Upper Cone site (Site U1528). 1: Photomicrograph under reflected light. 2: The same grain etched for 90s using NaOCl. 3: Analytical transects of SIMS points shown in image 2 (red, blue and green dots). The shaded green area represents ±1σ and the green line is the median. **a1** Core section 23R1. A euhedral pyrite grain with a late, fine-grained pyrite overgrowth. **a2** Pyrite showing oscillatory zonation that is parallel to the grain margin with an overgrowth of fine-grained pyrite that appears blue-green in color. **a3** All $\delta^{34}S$ values plot within error of, or below, 0‰ with the core of the grain slightly enriched in ^{34}S compared to the margin. **b1** Core section 49R2. Pyrite is subhedral with a porous region containing anhydrite inclusions. **b2** The grain does not show any internal zonation when etched. **b3** All $\delta^{34}S$ values are below 0‰ with the area that is inclusion-rich containing the lowest $\delta^{34}S$ values.

Figure 6: Pyrite from chlorite-rich alteration at the NW Caldera site. 1: Photomicrograph under reflected light. 2: The same grain etched for 90s using NaOCl. 3: Analytical transects of SIMS points shown in image 2 (red, blue and green dots). The shaded green area represents ±1σ and the green line is the median. **a1** Core section 1R1. Pyrite shows a resorbed inner core overgrown by multiple generations of pyrite forming an inner porous zone and an outer massive zone. **a2** The etched grain shows multiple growth zones, mostly

within the outer zone. **a3** The grain core contains the lowest $\delta^{34}S$ values compared to the inner zone that contains higher values. **b1** Core section 5R1A. Euhedral pyrite overgrown at its margins by a late generation pyrite. **b2** The contact between early pyrite and late pyrite is delineated by a blue-yellow color with multiple zonation seen in the late pyrite. **b3** The core of the euhedral grain contains higher $\delta^{34}S$ values compared to g margin. The zone that appears blue-yellow in B2 contains the highest $\delta^{34}S$ values that decrease toward the grain margin. **c1** Core section 5R1B. Euhedral pyrite grain. **c2** The core of the grain appears yellow-blue, with oscillatory zonation present. **c3** The core of the grain contains high $\delta^{34}S$ values relative to the margin. d1 Core section 83R1. Subhedral pyrite grain. **d2** Weak oscillatory zonations in the center of the grain and a sub-grain of pyrite that appears yellow-orange in color. **d3** $\delta^{34}S$ values decrease across the grain with only a single point greater than 0‰.

Figure 7: Pyrite grains from pyrophyllite + illite alteration at the NW Caldera. 1: Photomicrograph under reflected light. 2: The same grain etched for 90s using NaOCl (RC = relict core). 3: Analytical transects of SIMS points shown in image 2 (red, blue and green dots). The shaded green area represents ±1σ and the green line is the median. **a1** Core section 55R1. Anhedral pyrite. **a2** No clear oscillatory zonation is visible - irregular bright zones occur in the core of the grain. **a3** All $\delta^{34}S$ values plot at <0‰, with the region of bright zonations having higher $\delta^{34}S$ values compared to the grain margin. **b1** Core section 65R1, grain A. The pyrite grain has an anhedral morphology and contains an inclusion of Fe-oxide (FeOx). **b2** Complex internal zonation delineated by orange zones, especially in the grain core. A sub-grain occurs in the upper part of the grain. **b3** A highly heterogeneous sulfur isotope composition with no clear trend with respect to the core, or margin of the grain. **c1** Close-up of the grain core shown in b2. The center of the core has undergone dissolution leaving a void. **c2** The core appears brighter in color with distinctive oscillatory changes in color. Towards the margin of the grain, the brighter zones become highly irregular. **c3** The "bright band" in image c2 coincides with a large excursion in $\delta^{34}S$ values from positive to negative. **d1** Core section 65R1, grain B. Subhedral coarse-grained pyrite. **d2** A relict core is delineated by oscillatory orange zonation. Irregular bright yellow-orange zonations are visible at the margin of the grain. **d3** The center of

the pyrite grain is enriched in ^{34}S relative to the margin. **e1** Core section 65R1, grain C. Anhedral pyrite grain. **e2** Etching shows oscillatory orange zones that delineate a relict core. **e3** The $\delta^{34}S$ composition is highly variable across the grain with a high $\delta^{34}S$ values in the core mantled by a zone of low $\delta^{34}S$ values that progressively increase toward the margin of the grain. RC = relict core.

Figure 8: Element distribution maps of pyrite from core section 23R1 of the Upper Cone site. **a** Cu, **b** Sb, **c** Se, **d** As, **e** Co. The highest relative Sb and Cu contents occur along oscillatory growth zones.

Figure 9: Element distribution maps of pyrite from core section 1R1 (a-c) and 5R1 grain A and B (d-f) from near-seafloor, chlorite-rich alteration (<30 mbsf) at the NW Caldera site. **a** As, **b** Sb, **c** Cu. Arsenic, Sb and Cu content is highest along boundaries between different pyrite generations. Copper occurs as mineral inclusions (Cp- chalcopyrite). **d** As, **e** Sb, **f** Cu. Arsenic content is high at the interface between the euhedral pyrite and later overgrowths. Antimony does not exhibit any visible zonation. Copper is slightly higher in pyrite overgrowths.

Figure 10: Element distribution maps of pyrite from core section 55R1 and 65R1 from a pyrophyllite-rich alteration zone at the NW Caldera site. **a-e** Core section 55R1. **a** Co, **b** As, **c** Cu, **d** Se, **e** Sb. Randomly oriented zones of high Co content occur in the core of the grain. No detectable zonation occurs for Cu, As, Se or Sb. **f-h** Core section 65R1, grain A. **f** Co, **f*** Co map of the grain core, **g** Cu, **h** As. The core of the grain has the highest Co content. Bright zones identified by etching are Co-rich. Copper does not correlate with Co content and is higher at the edge of the grain. **i-k** Core section 65R1; grain B. **i** Co, **j** As, **k** Cu. The core of the grain has high As and Cu contents and is mantled by a zone of high Co content. Cobalt is also enriched in zones that contain bright orange zonation when etched. **l-p** Core section 65R1, grain C. **l** Co, **m** As, **n** Cu, **o** Se, **p** Sb. The core of the grain is enriched in Co with Co-rich oscillatory zonation that correlates with bright orange bands in the etched image. Arsenic, Se and Sb do not show any internal variation. Cu occurs as mineral inclusions (Cp= chalcopyrite).

Figure 11: Summary of pyrite sulfur isotope data for Brothers volcano. The variation in $\delta^{34}S$ values across individual pyrite grains is greater than the total amount of variation from all bulk rock analyses. Pyrite from pyrophyllite + illite samples shows the most inter-grain variation (Bulk Py: de Ronde et al. 2003, 2005, 2011; SIMS Py: Martin et al. 2022a). Boxes = upper and lower quartile, black line = median, X = average, circles = data points, whiskers = minimum and maximum.

Figure 12: Schematic summary of key processes that influence the distribution of trace metals and sulfur isotope composition of pyrite at Brothers volcano. NW Caldera: **a** Exsolution of a magmatic brine (~40 wt.% NaCl equivalent; de Ronde et al. 2019a) directly from a volatile-saturated magma. **b** Dilution of magmatic brine by seawater-derived hydrothermal fluids and precipitation of pyrite with Co-enriched cores with $\delta^{34}S$ values >0‰. Pyrite grains undergo dissolution leading to an anhedral morphology. Disproportionation of degassing SO_2 is ongoing. **c** Pyrite from chlorite-rich alteration does not show pronounced internal zonations due to fluid overprinting and metal remobilization; sulfur is sourced from TSR, leaching of host rocks and SO_2 disproportionation. **d** Near seafloor pyrite (<30 mbsf) contains As (Sb)-rich zones with $\delta^{34}S$ values >0‰ produced during shallow subseafloor mixing of seawater with hydrothermal fluid. Upper Cone: **e** Formation of pyrite with no visible zonation with $\delta^{34}S$ values that are <0‰, indicating sulfur is sourced primarily from magmatic volatile degassing where SO_2 undergoes disproportionation. Magmatic fluids are low-salinity and have a low potential to transport metals. **f** Some pyrite grains exhibit oscillatory zonation with a coupled relationship between Cu and Sb that is linked to magmatic volatile influx. Sulfur isotope ratios are <0‰ but have higher values than samples located deeper in the system, reflecting the addition of some sulfur from TSR and leaching of wall rocks.

Table Captions

Table 1: Summary of the sulfur isotopic composition of pyrite grains analyzed in this study. *denotes all analyses for the mineral grain – see Figure 7. Nalu + Prl = natroalunite + pyrophyllite, Chl + Qtz = chlorite

+ quartz, Prl + Ill = pyrophyllite + illite. For an example of magmatic pyrrhotite grains analyzed, see ESM 3. Full data in ESM, Table A1.

Table_1

Sample/Location	*n*	Median (‰)	Average (‰)	σ	Max (‰)	Min (‰)
Upper Cone – Nalu + Prl						
23R1	11	-1.4	-1.5	1.1	0.2	-3.4
49R2	15	-5.9	-6.1	1.3	-4.2	-8.1
NW Caldera – Chl + Qtz						
1R1	12	-1.1	-1.1	2.1	1.7	-4.5
5R1 (A)	9	-0.5	0.0	2.1	3.4	-2.6
5R1 (A)	5	0.2	0.5	1.2	1.8	-1.6
83R1	14	-4.0	-3.9	2.4	0.7	-7.5
NW Caldera – Prl + Ill						
55R1	14	-3.2	-3.9	2.2	-1.0	-8.9
65R1-A	8	-2.9	-2.9	3.0	1.2	-6.9
All analyses (65R1-A)	*(14*)*	*(-2.9)*	*(-2.4)*	*(3.0)*	*(2.8)*	*(-6.9)*
65R1-A-Core	9	1.3	1.3	1.9	4.1	-2.1
65R1-B	9	3.3	1.3	3.0	4.0	-5.9
All analyses (65R1-B)	*(14*)*	*(3.3)*	*(0.7)*	*(4.0)*	*(4.0)*	*(-5.9)*
65R1-C	17	-0.1	-0.6	2.8	4.6	-5.3
Magmatic sulfide blebs						
Unaltered samples	15	0.2	0.9	2.4	6.7	-3.1

Fig_1

Click here to access/download;Figure;Fig_1.jpg

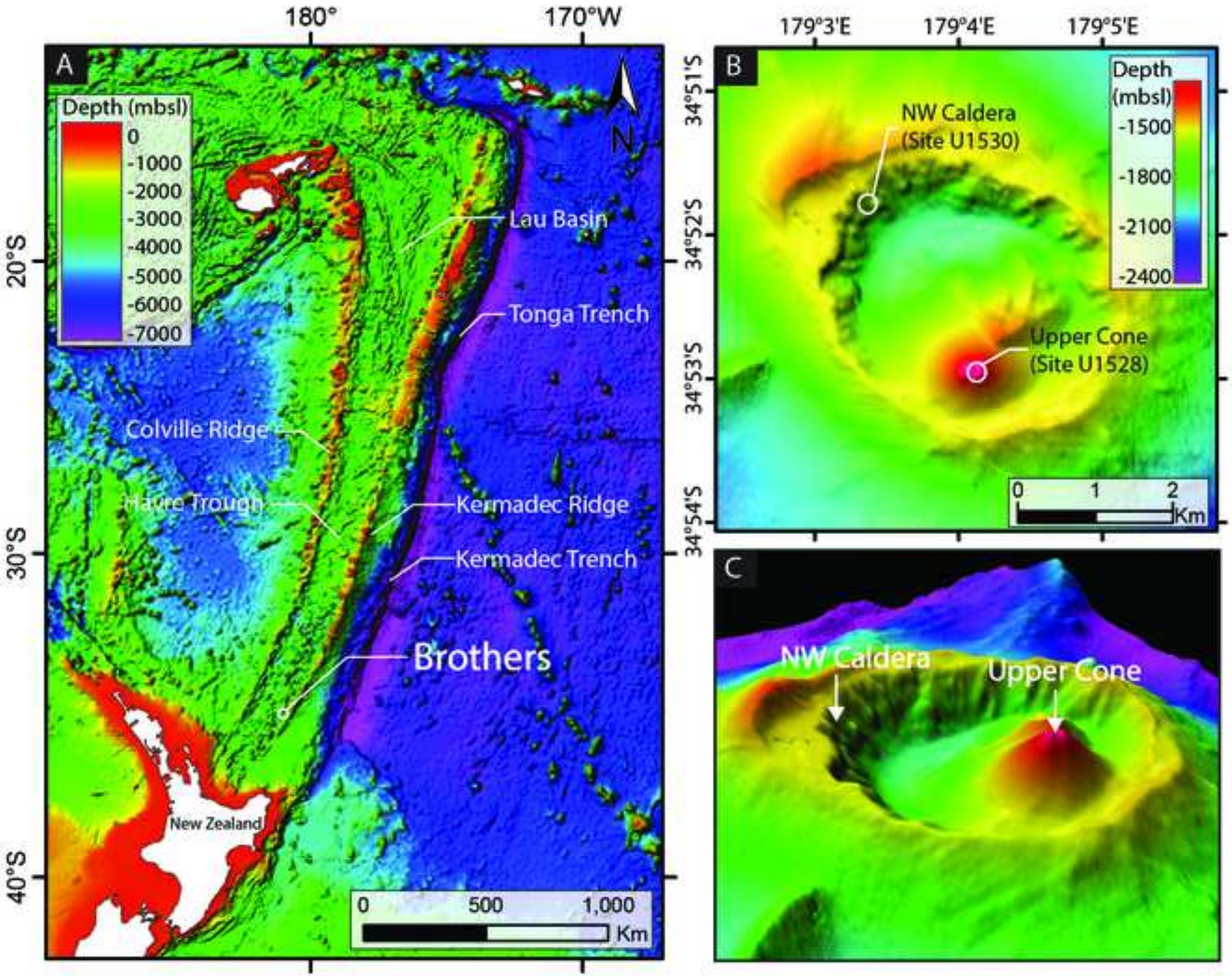

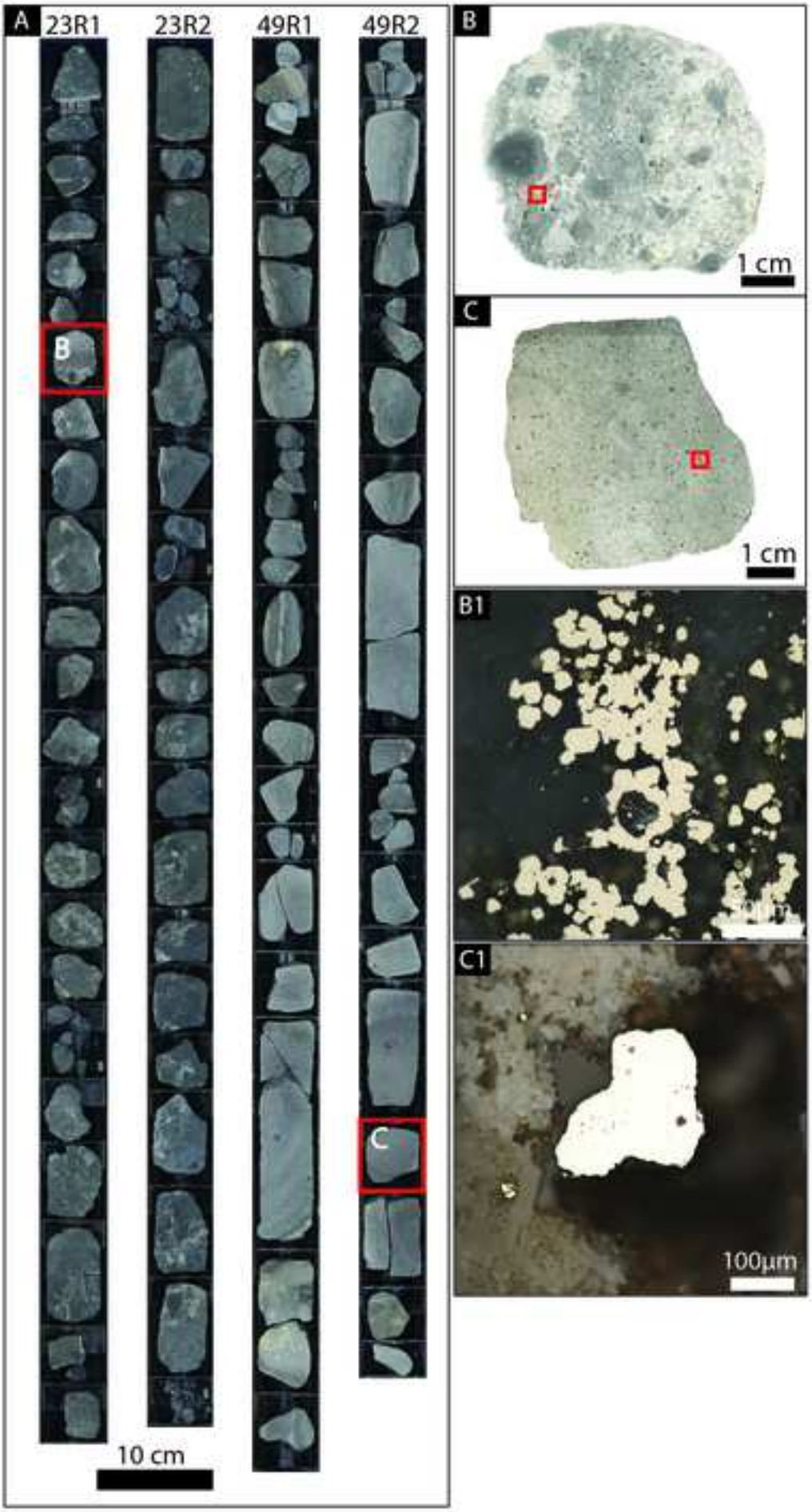
A
23R1
23R2
49R1
49R2
B
C
10 cm
B
1 cm
C
1 cm
B1
C1
100µm

Fig_3

Click here to access/download;Figure;Fig_3_REV.jpg

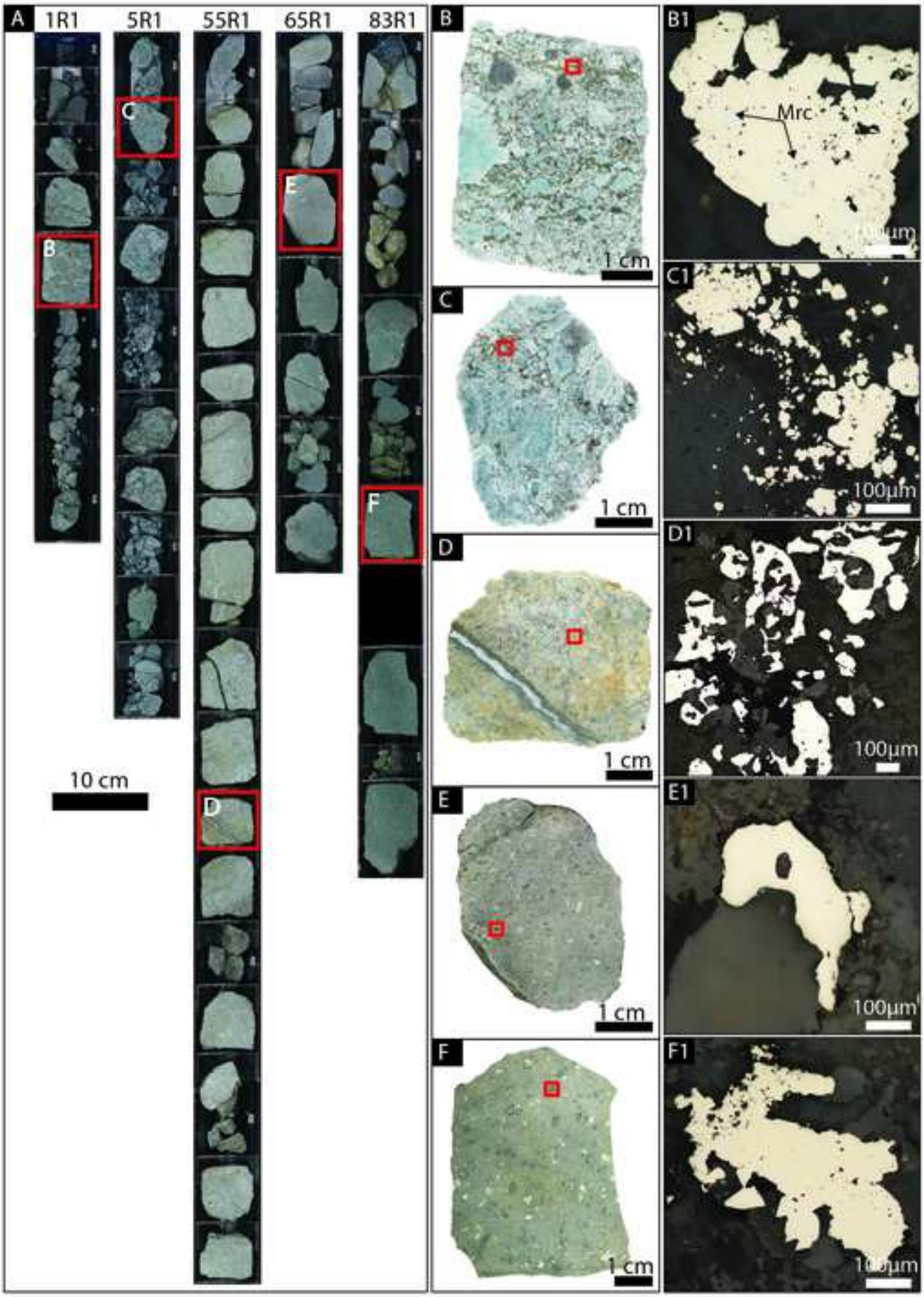

Fig_4

Click here to access/download;Figure;Fig_4.jpg

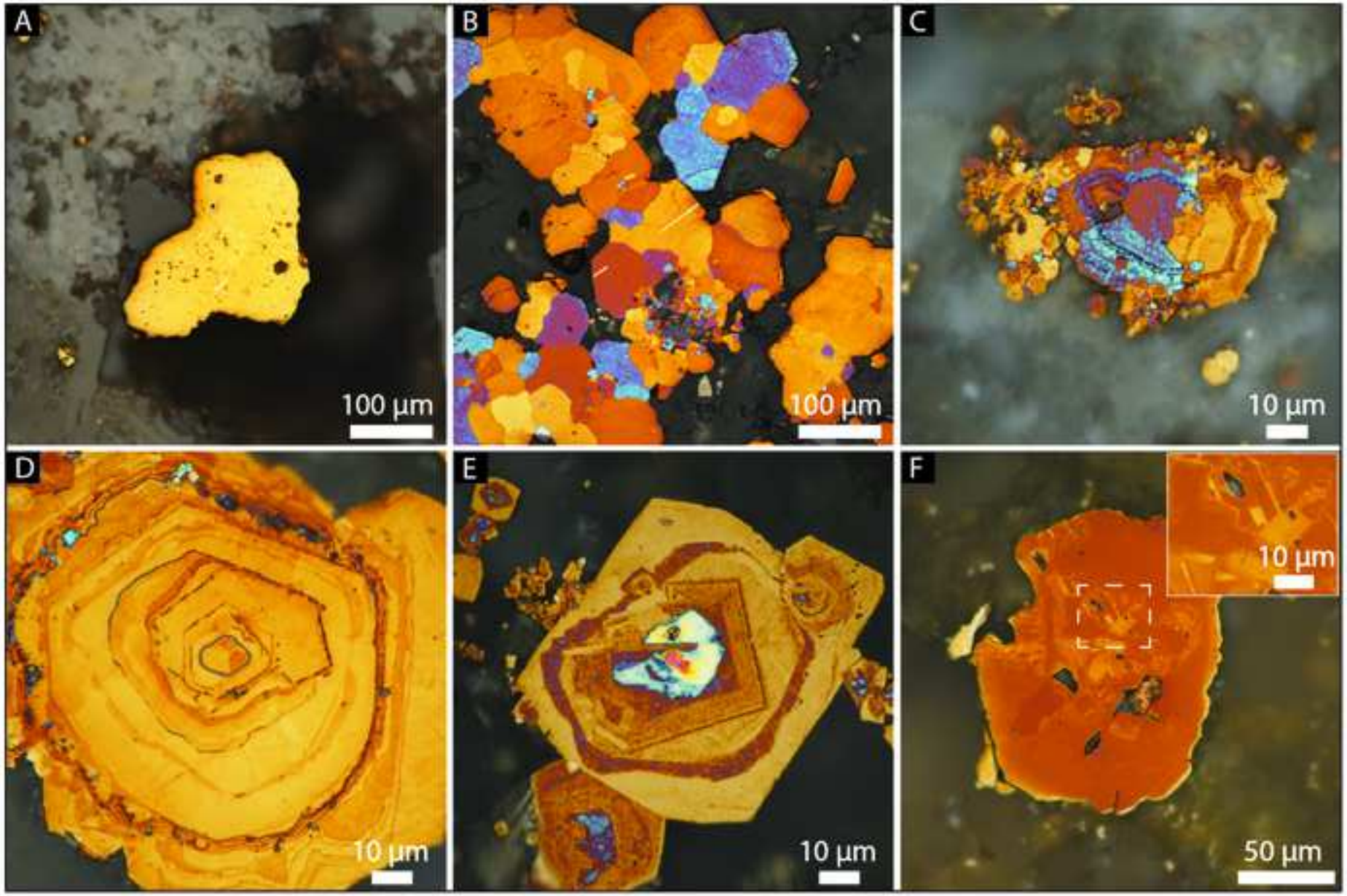

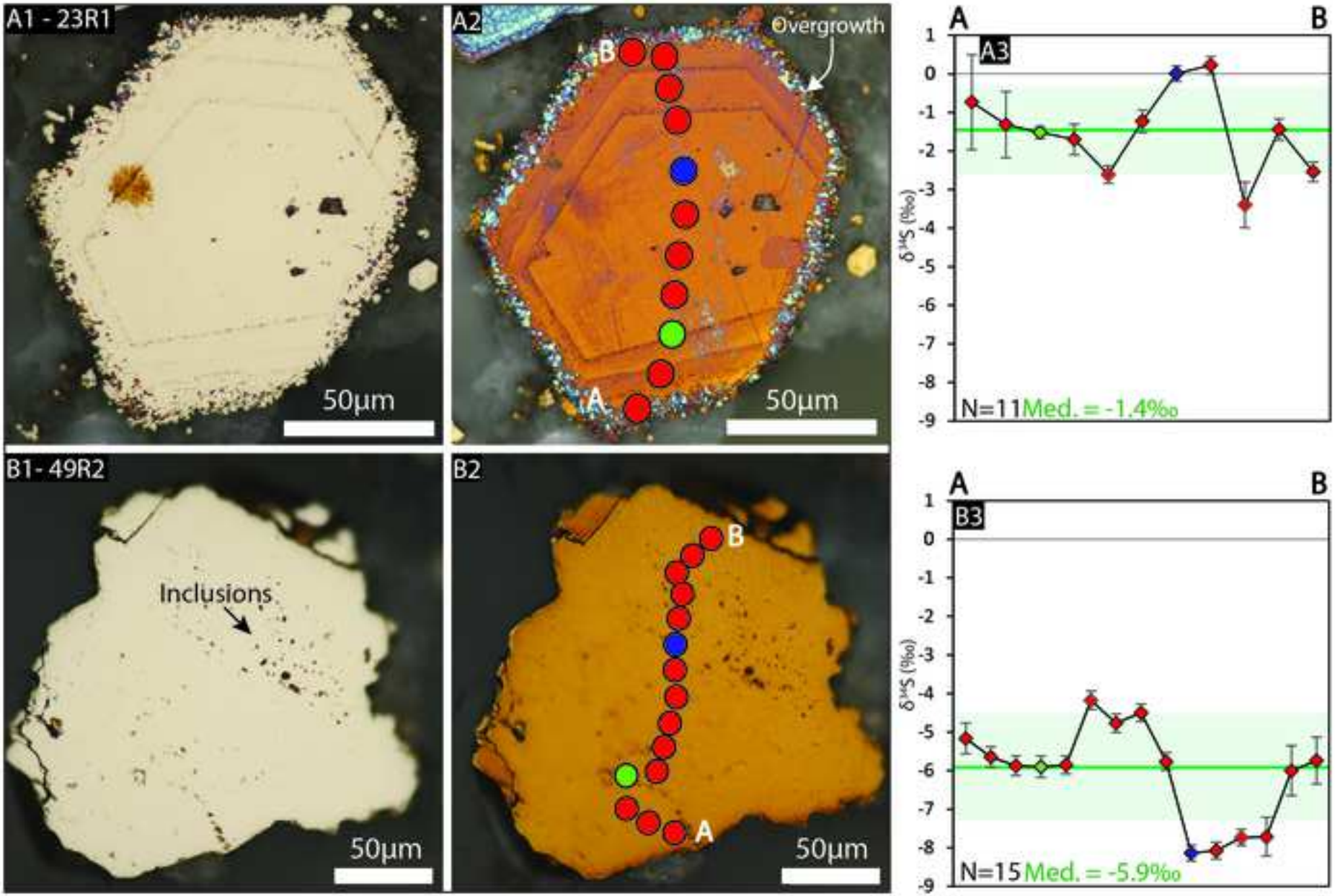
A1 - 23R1
50µm
A2
Overgrowth
B
A
50µm
A
B
A3
δ³⁴S (‰)
N=11 Med. = -1.4‰
B1- 49R2
Inclusions
50µm
B2
B
A
50µm
A
B
B3
δ³⁴S (‰)
N=15 Med. = -5.9‰

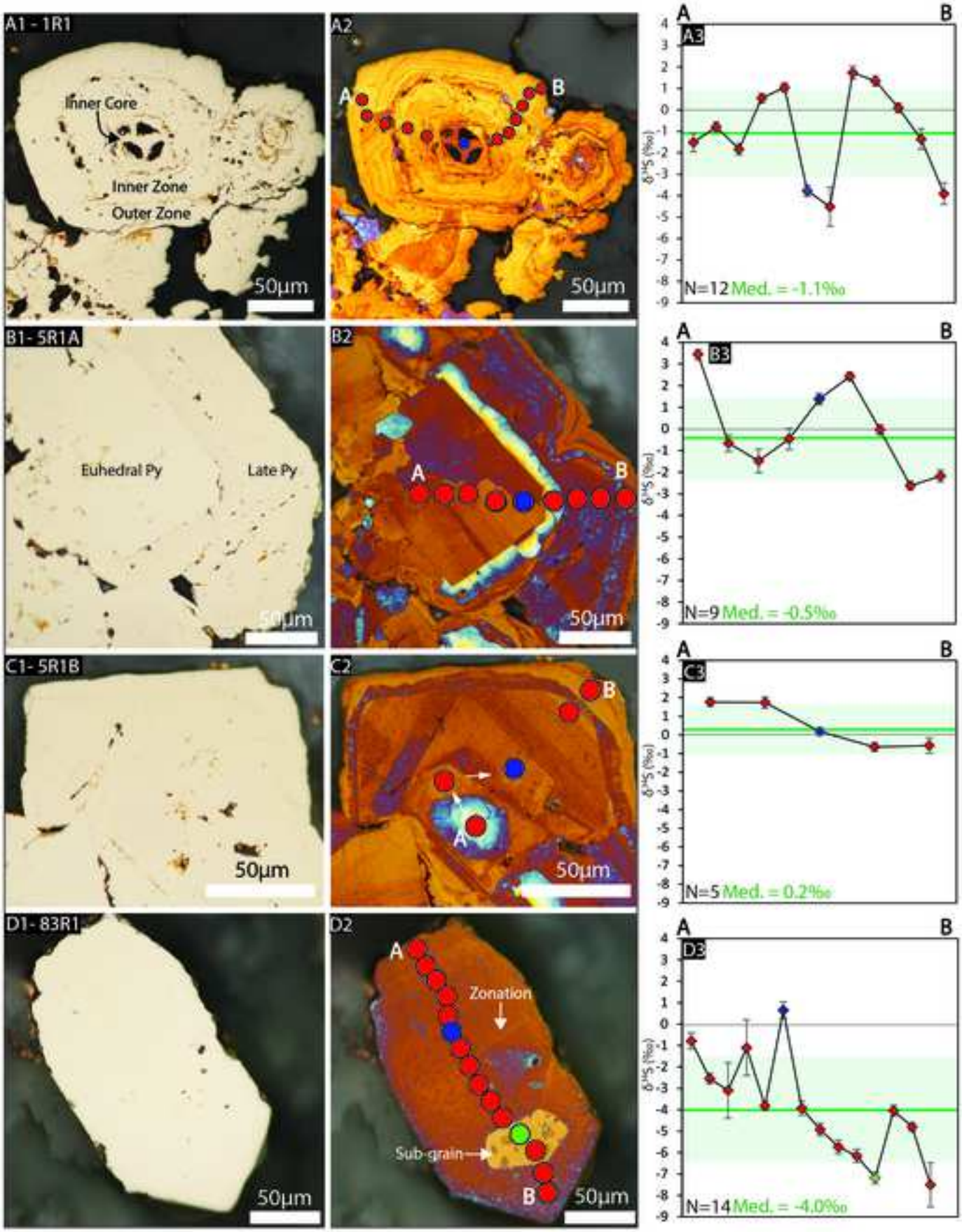
A1 - 1R1
Inner Core
Inner Zone
Outer Zone
50µm
A2
A
B
50µm
A3
N=12 Med. = -1.1‰
B1 - 5R1A
Euhedral Py
Late Py
50µm
B2
A
B
50µm
B3
N=9 Med. = -0.5‰
C1 - 5R1B
50µm
C2
B
A
50µm
C3
N=5 Med. = 0.2‰
D1 - 83R1
50µm
D2
A
Zonation
Sub-grain
B
50µm
D3
N=14 Med. = -4.0‰

Fig_7A

Click here to access/download;Figure;Fig_7A.jpg

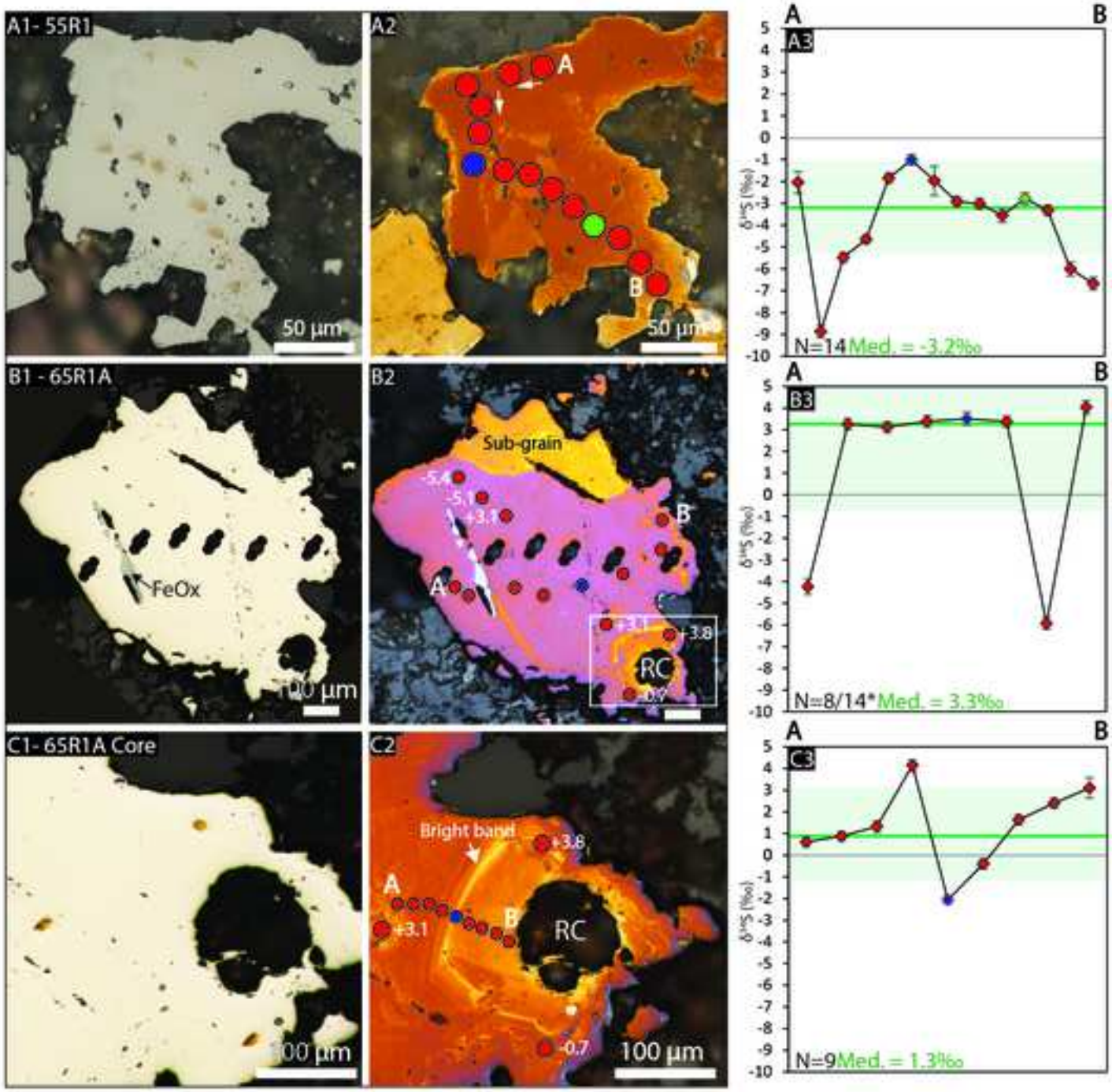

Fig_7B

Click here to access/download;Figure;Fig_7B.jpg

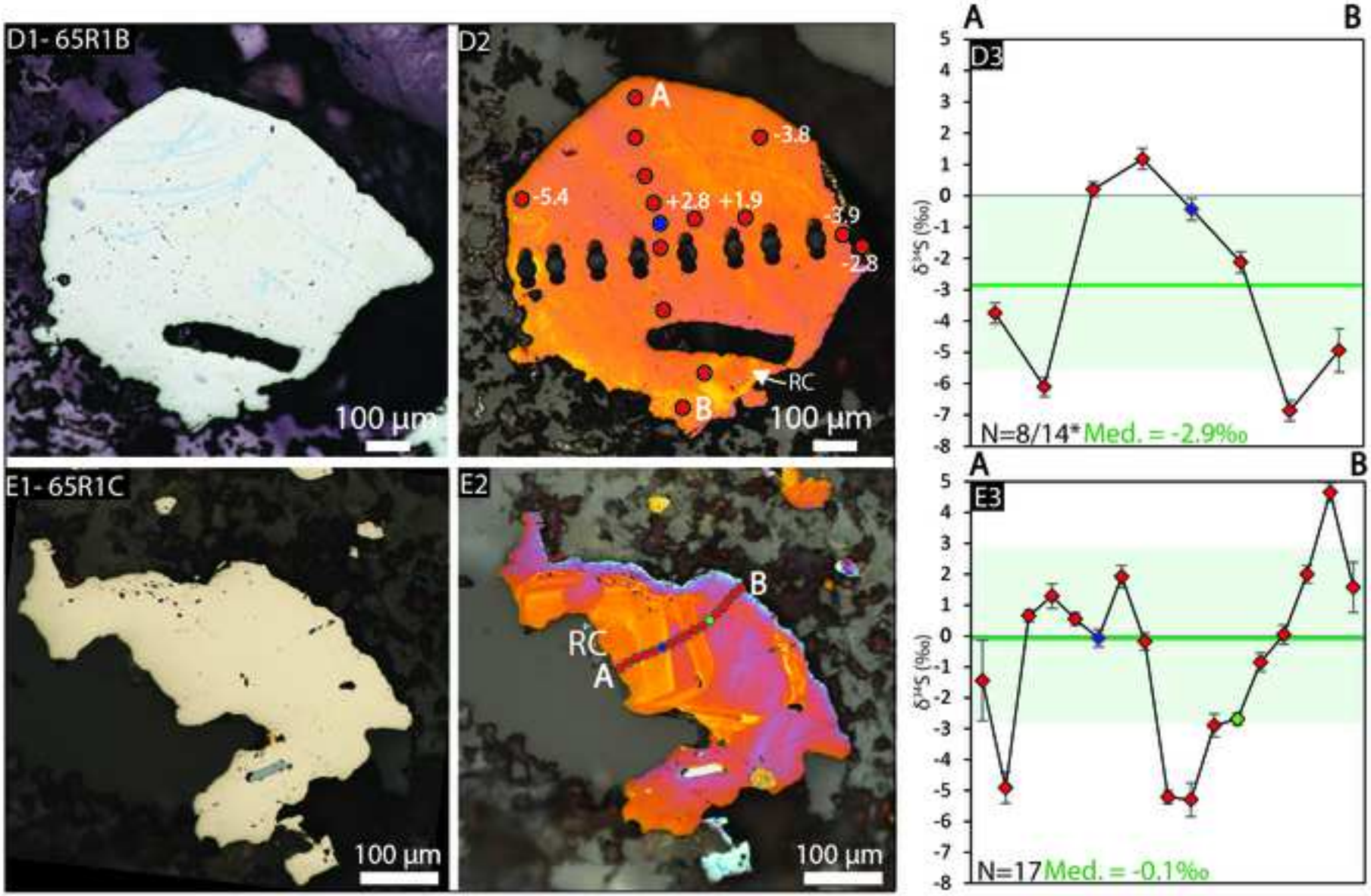

Fig_8

Click here to access/download;Figure;Fig_8.jpg

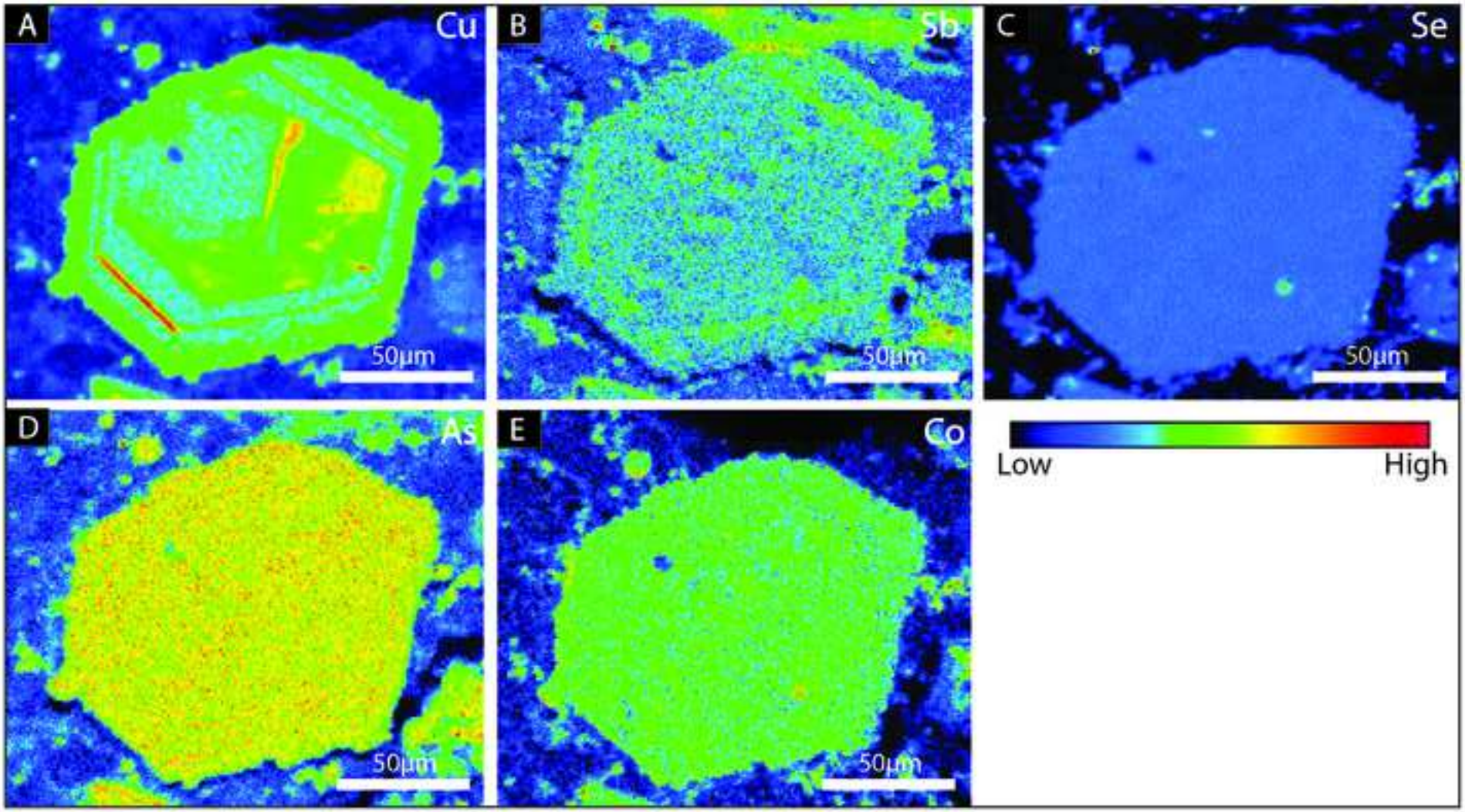

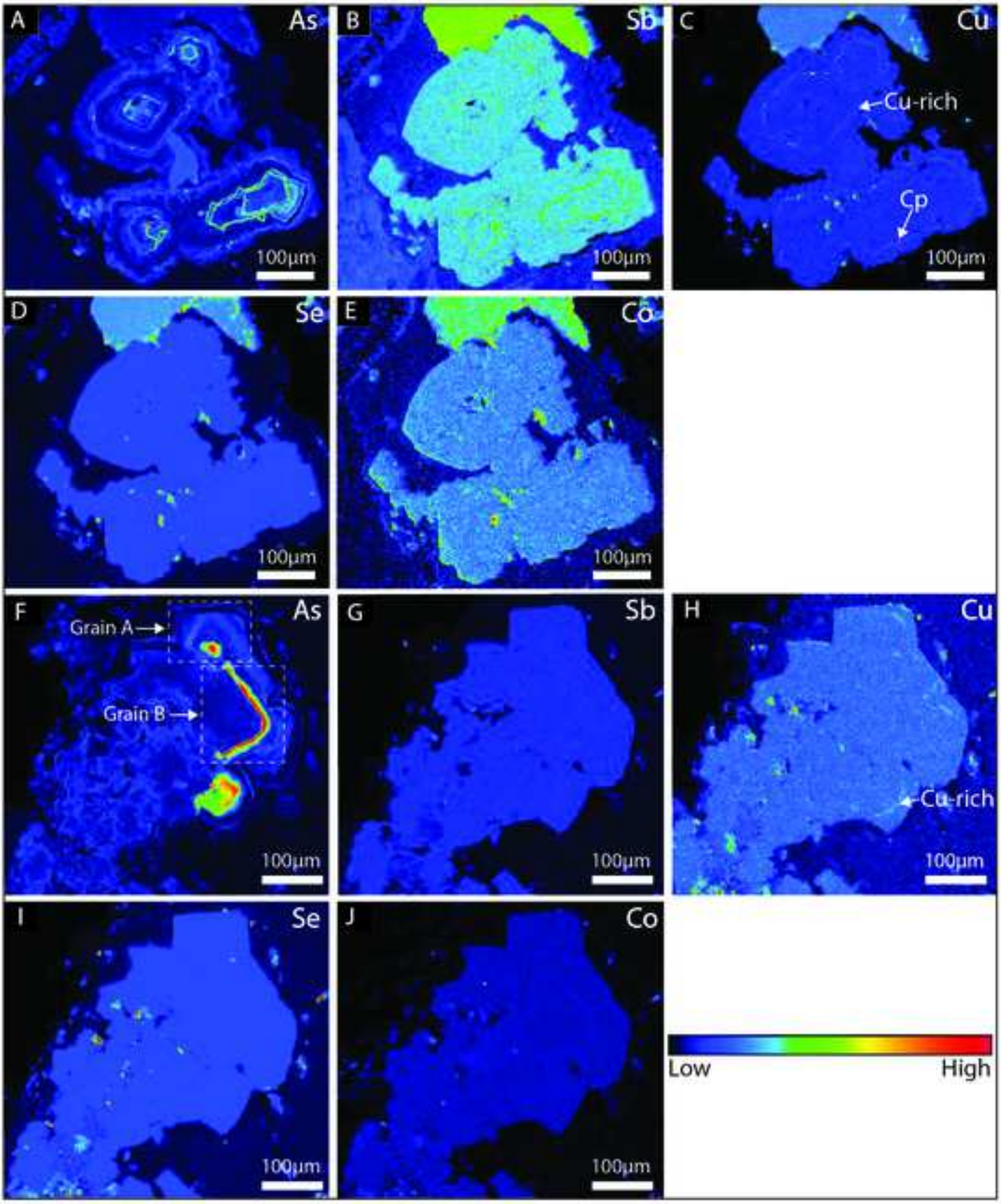
A
As
100µm
B
Sb
100µm
C
Cu
Cu-rich
Cp
100µm
D
Se
100µm
E
Co
100µm
F
As
Grain A
Grain B
100µm
G
Sb
100µm
H
Cu
Cu-rich
100µm
I
Se
100µm
J
Co
100µm
Low
High

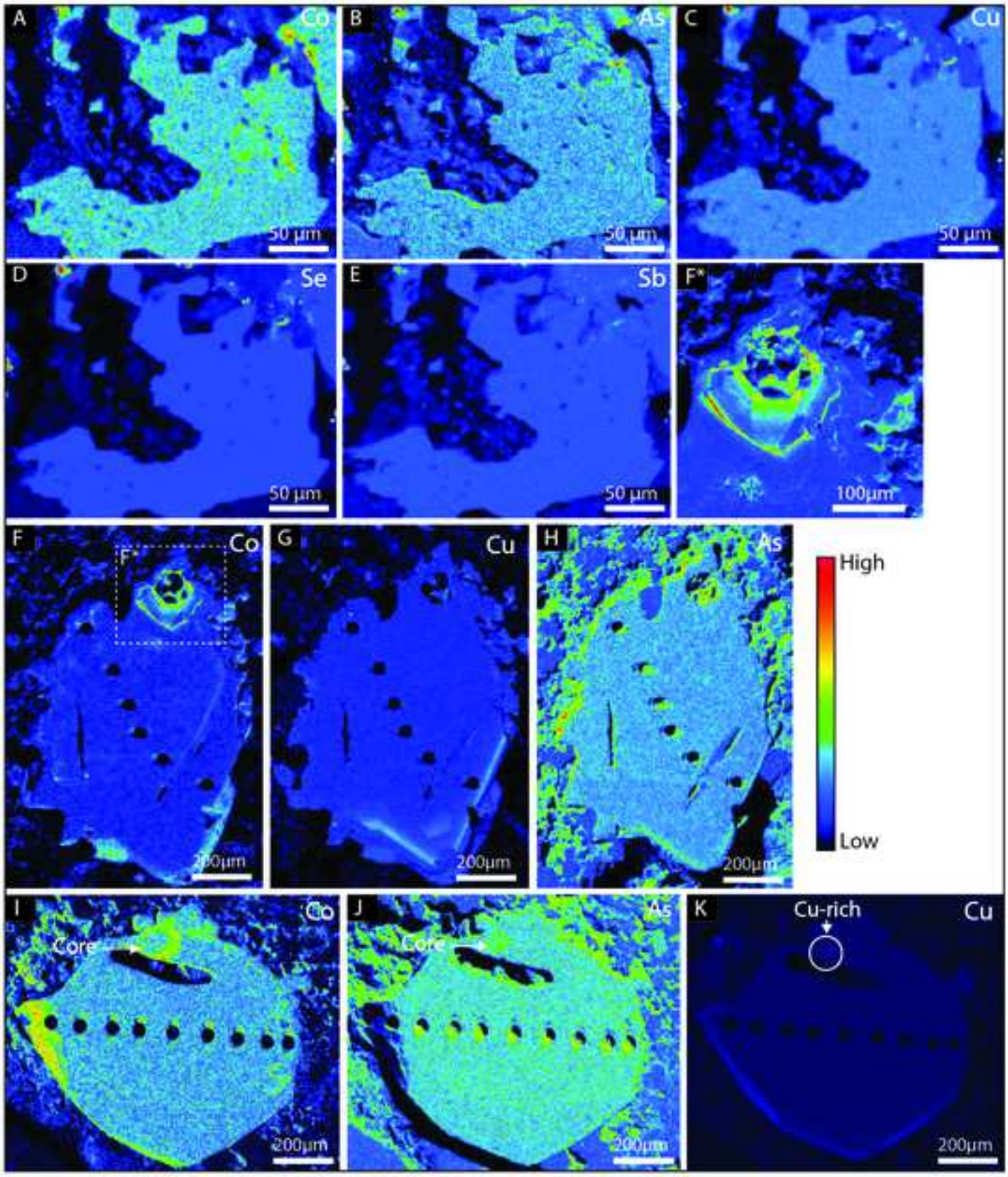
A
Co
50 µm
B
As
50 µm
C
Cu
50 µm
D
Se
50 µm
E
Sb
50 µm
F*
100µm
F
Co
F*
200µm
G
Cu
200µm
H
As
200µm
High
Low
I
Co
Core
200µm
J
As
Core
200µm
K
Cu-rich
Cu
200µm

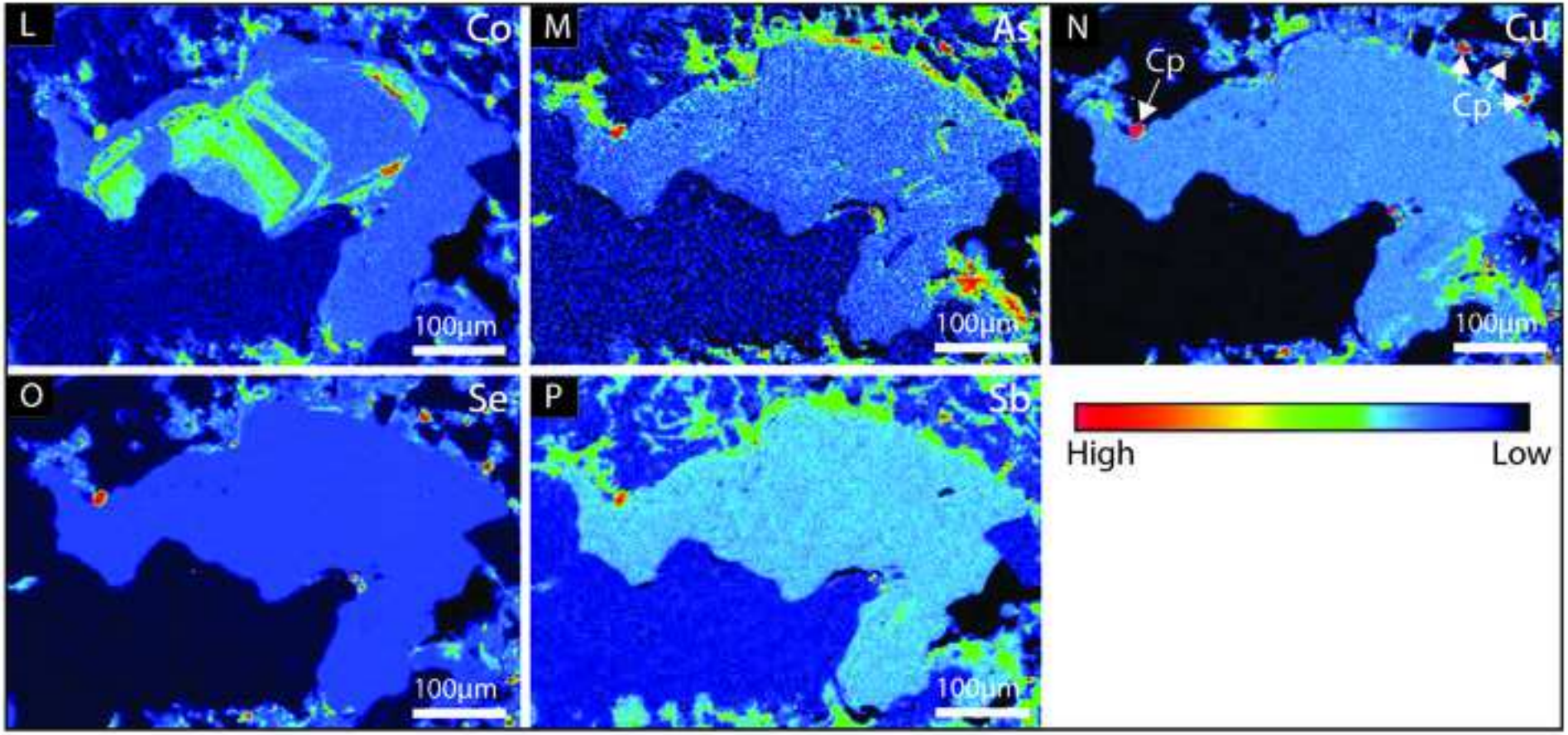
L
Co
100µm
M
As
100µm
N
Cu
Cp
Cp
100µm
O
Se
100µm
P
Sb
100µm
High
Low

Fig_11

Click here to access/download;Figure;Fig_11.jpg

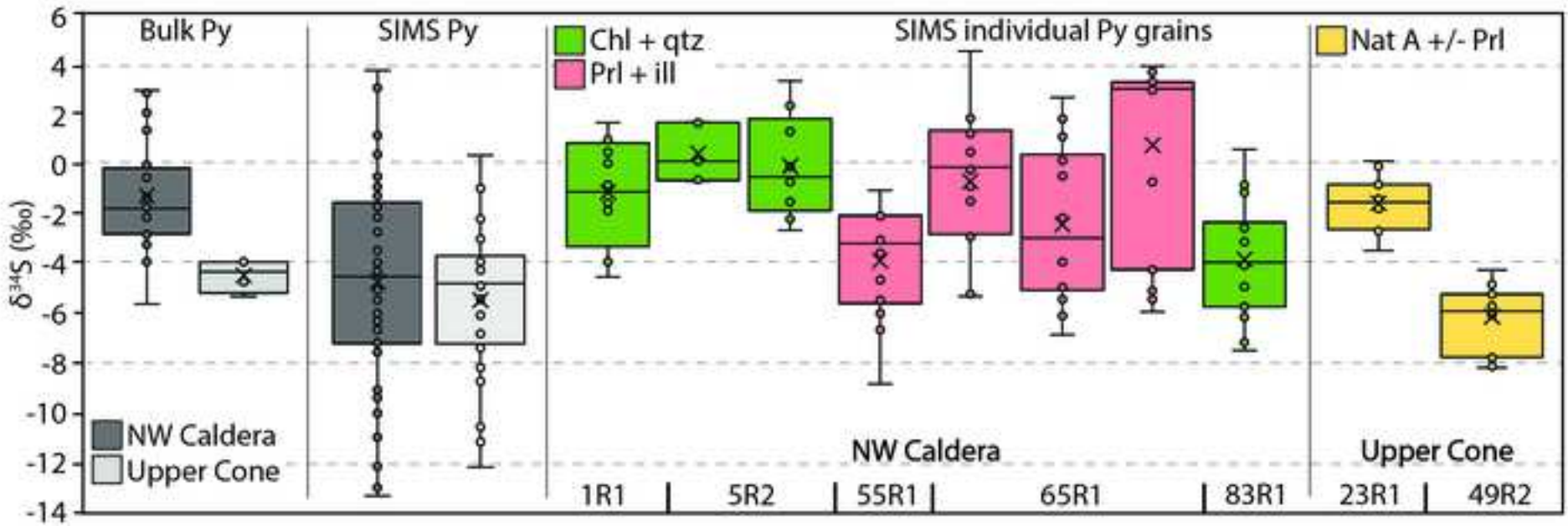

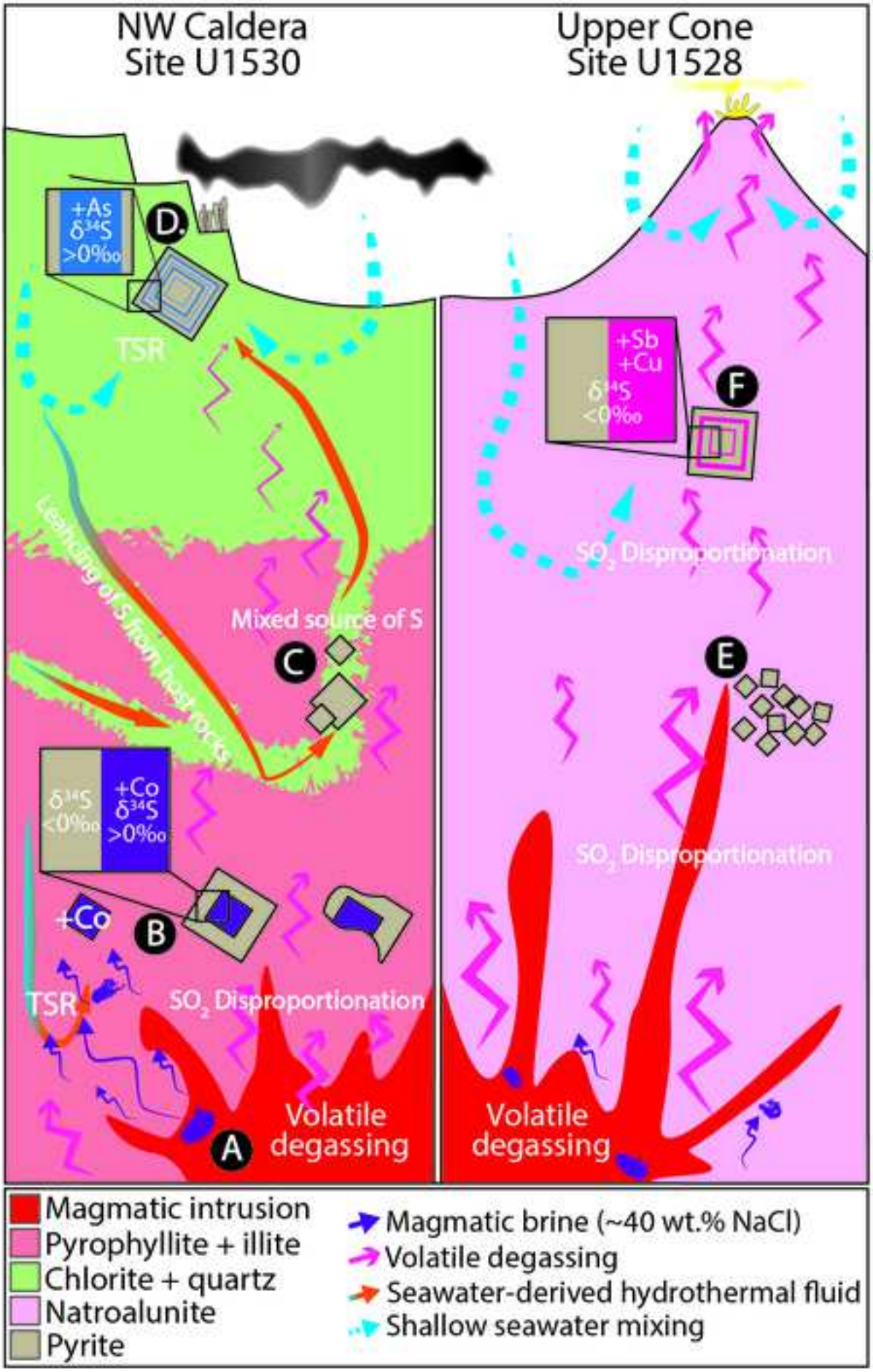
NW Caldera
Site U1530
Upper Cone
Site U1528
+As
δ34S
>0‰
D
TSR
Leaching of S from host rocks
Mixed source of S
C
δ34S
<0‰
+Co
δ34S
>0‰
+Co
B
TSR
SO2 Disproportionation
Volatile degassing
A
+Sb
+Cu
δ34S
<0‰
F
SO2 Disproportionation
E
SO2 Disproportionation
Volatile degassing
Magmatic intrusion
Pyrophyllite + illite
Chlorite + quartz
Natroalunite
Pyrite
Magmatic brine (~40 wt.% NaCl)
Volatile degassing
Seawater-derived hydrothermal fluid
Shallow seawater mixing

Click here to access/download
Supplementary Material
Martin_et_al_ESM_Table A1 and A2.xlsx

Click here to access/download
Supplementary Material
ESM_3.pdf